Long-term airborne measurements of pollutants over the UK, ~~including during the COVID-19 pandemic,~~ to support air quality model development and evaluation

Angela Mynard[1], Joss Kent[1], Eleanor R Smith[1], Andy Wilson[1], Kirsty Wivell[1], Noel Nelson[1], Matthew Hort[1], James Bowles[1], David Tiddeman[1], Justin M. Langridge[1], Benjamin Drummond[1] and Steven J. Abel[1]

[1]Met Office, Exeter, Devon, EX3 1PB, UK

Correspondence to: Angela Mynard (angela.mynard@metoffice.gov.uk)

Abstract

The ability of regional air quality models to skilfully represent pollutant distributions throughout the atmospheric column is important to enabling their skilful prediction at the surface. This provides a requirement for model evaluation at elevated altitudes, though observation datasets available for this purpose are limited. This is particularly true of those offering sampling over extended time periods. To address this requirement and support evaluation of regional air quality models such as the UK Met Offices Air Quality in the Unified Model (AQUM), a long-term, quality assured, dataset of the three-dimensional distribution of key pollutants has been collected over the southern United Kingdom from July 2019 to April 2022.~~June 2019 to April 2022. This sampling period encompasses operations during the global COVID-19 pandemic, and as such the dataset serves an additional application in providing a unique resource with which to explore changes in atmospheric composition associated with reduced emissions during this period.~~ Measurements were collected using the Met Office Atmospheric Survey Aircraft (MOASA), a Cessna-421 instrumented for this project to measure gaseous nitrogen dioxide, ozone, sulphur dioxide and fine mode ($PM_{2.5}$) aerosol. This paper introduces~~provides a technical introduction to~~ the MOASA measurement platform, flight strategies and instrumentation and is not intended to be an in-depth diagnostic analysis, but rather a comprehensive technical reference for future users of these data.~~.~~ The MOASA air quality dataset includes 63 flight sorties (totalling over 150 hours of sampling), the data from which are openly available for use. To illustrate potential uses of these upper air observations for regional-scale model evaluation, example~~Example~~ case studies ~~using data from these sorties~~ are presented, which include ~~an~~ analysis of the spatial scales of measured pollutant variability, ~~a comparison of airborne to ground-based observations over Greater London and~~ initial work to evaluate performance of the AQUM regional air quality model~~. These case studies show that for observations of relative humidity, nitrogen dioxide and particle counts, natural pollutant variability is well~~, and an introduction to the vertical structure of pollutants observed ~~by the aircraft, whereas SO_2 variability is limited by instrument precision. Good agreement is seen between observations aloft and those on the ground, particularly for $PM_{2.5}$. ($r^2 = 0.90$). Analysis of odd oxygen suggests titration of ozone is the dominant chemical process throughout~~during repeated flight patterns over Greater London, including during the column for the flights analysed, although a slight enhancement of ozone aloft is seen. Finally, a preliminary evaluation of AQUM performance for two case-studies suggests a large positive model bias for ozone aloft, coincident with a negative

model bias for NO_2 aloft. On one case, there is evidence that an under prediction in the modelled boundary layer height contributes to the observed biases at elevated altitudes.~~COVID-19 impacted period.~~

~~1 Introduction~~

1 Introduction

The World Health Organisation identifies atmospheric air pollution as the single largest environmental risk to human health globally (World Health Organization, 2017). Long-term exposure to anthropogenic air pollution is linked with increased morbidity rates and premature mortality from chronic diseases (Air Quality Expert Group, 2020, Manisalidis et al., 2020),~~,~~ which in the UK alone is estimated to have an annual impact on shortening lifespans equivalent to 28 – 36 thousand deaths (DEFRA, 2019). The impacts of air pollution on human health can be most acute in urban areas, particularly megacities, where high pollutant concentrations coincide with high population densities (Molina and Molina, 2004). In addition to impacting human health, air pollution has been shown to have wider detrimental impacts on ecosystems, including animal welfare, crop yields, waterways, biodiversity and visibility (DEFRA, 2019).

From an atmospheric sciences perspective, air pollution is a complex, transboundary problem. Gaseous and particulate pollutants originate from many sources, are subject to transport and mixing over a range of scales and undergo complex physical and chemical processing prior to deposition. In order to develop effective strategies for mitigating the impacts of air pollution, for example through emission control and limiting population exposure, these processes must be understood and leveraged to provide predictive capability extending spatially and temporally beyond the ground-truth provided by observations. Atmospheric chemical transport models represent a key tool in this domain.

Air quality models vary widely in spatial scale and complexity and have evolved rapidly in sophistication in recent years. The reader is directed to El-Harbawi (2013) for a comprehensive review of air quality modelling systems, that span scales from street canyon to global and incorporate a wide range of schemes representing pollutant emissions, turbulent mixing, advection, gas-phase chemistry and aerosol processes. Many of these models run online, meaning meteorological and pollutant fields evolve prognostically within the modelling system allowing feedbacks between the two to be represented (such as direct and indirect aerosol effects) (Savage et al., 2013).

In the Met Office, the primary air quality modelling system is the Air Quality in the Unified Model, AQUM, a 12 km limited area forecast configuration of the Met Office Unified Model (MetUM). AQUM provides daily UK national air quality forecasts of the Daily Air Quality Index (DAQI) up to five days ahead (see https://uk-air.defra.gov.uk/forecasting/), generated from the forecast of nitrogen dioxide (NO_2), sulphur dioxide (SO_2), ozone (O_3) and particulate matter (diameters (Dp) <2.5 µm: $PM_{2.5}$ and Dp <10 µm: PM_{10}) concentrations. AQUM has 8 vertical levels up to a model top height of 39 km and mixing is parameterised throughout the full depth of the troposphere using a non-local, first order closure, multi-regime scheme (Lock et al., 2000). Given the resolution of AQUM, it is best suited to modelling background and regional air quality away from strong, very localised sources of pollution (Neal et al., 2017, Williams et al., 2018). A comprehensive description of the AQUM is available in Savage et al. (2013).~~In the Met Office, the primary air quality modelling system is the Air Quality in the Unified Model, AQUM, a limited area forecast configuration of the Met Office Unified Model (MetUM)~~

~~(Savage et al., 2013, Walters et al., 2019). AQUM provides daily UK national air quality forecasts of the Daily Air Quality Index (DAQI) up to five days ahead (see). The DAQI is generated from the forecast of nitrogen dioxide (NO_2), sulphur dioxide (SO_2), ozone (O_3) and particulate matter (diameters (Dp) <2.5 µm: $PM_{2.5}$ and Dp <10 µm: PM_{10}) concentrations. The AQUM 12 km horizontal resolution grid covers much of western Europe (Savage et al., 2013) with 63 vertical levels up to a top height of 39km, where levels are non uniform and the vertical resolution becomes coarser away from the surface. AQUM derives its boundary conditions from the MetUM global forecast model (meteorological fields) and GEMS/MACC global models (chemistry and aerosol fields) (Flemming et al., 2009). Within the model domain, emissions over the UK are derived from the UK National Atmospheric Emissions Inventory (NAEI, (Thistlethwaite et al., 2013)), which has a resolution of 1 km. Atmospheric chemistry is represented by the UK Chemistry and Aerosols (UKCA) Regional Air Quality chemistry scheme (OConnor et al., 2014), and aerosol processes by the Coupled Largescale Aerosol Simulator for Studies in Climate (CLASSIC) scheme (Bellouin et al., 2011). Given the resolution of AQUM, it is best suited to modelling background and regional air quality away from strong, very localised sources of pollution. A comprehensive description of the AQUM is available in Savage et al. (2013).~~

Air quality models, including AQUM, require high quality observations for development and evaluation. Given that air quality regulatory limits are imposed at ground level only, air quality model evaluation studies typically focus on assessment of performance using surface measurements. In the UK, these observations are commonly provided by the Automatic Urban and Rural Network (AURN), an automatic ground monitoring network operated on behalf of the UK Department of Environment, Food and Rural Affairs ~~(DEFRA)~~ (Yardley et al., 2012).

Comparisons~~In a comparison~~ of AQUM to AURN observations ~~(,~~ Savage et al. (2013), Neal et al., (2017)), ~~)~~ found that AQUM generally performed well, in particular for large air quality events, but had a number of systematic biases. For example, a positive bias in ozone at urban sites, a positive~~/negative nitrogen oxide (NO_2)~~ NO_x bias at rural~~/ sites and a negative bias at~~ urban sites and small~~general~~ negative biases in ~~both~~ $PM_{2.5}$. These findings are generally comparable to similar air quality model evaluations that employ AURN observations, such as Williams et al., 2018 (10 km CMAQ-Urban model) and Neal et al., 2017 (HadGEM3-RA 50 km regional composition-climate model), although the latter showed a small positive bias in modelled $PM_{2.5}$. For AQUM, ground ~~and PM_{10}. Ground~~ based observations are used to bias-correct the model data and minimise some of these systematic biases at the surface (Neal et al., 2014). Models that require bias correcting through assimilation with observations have the potential to introduce bias into future predictions, as assumptions that the same factors apply both now and in the future can~~We note that these biases may not solely~~ be incorrectly made (Williams et al., 2018). We note that these biases may not solely~~due to model performance and could also~~ be ~~due to model performance and could also be~~ partially attributable to difficulties in evaluating a 12 km resolution model with point observations that have limited spatial coverage, both in the horizontal (raising questions of representivity) and in the vertical (limiting model evaluation away from the surface-atmosphere boundary). These limitations in observational data currently available for model evaluation provide motivation for the current work, with a particular focus on the need for observations away from the surface. Given that vertical mixing serves to transport pollutants both away-from and towards the surface, and pollutant chemical, physical and removal processes occur throughout the atmospheric column, model skill in this domain is critical to achieving successful prediction at the surface (Solazzo et al., 2013).

Observations of pollutants throughout the atmospheric column are increasingly available from satellite instruments (e.g. Tropomi on ESAs Sentinel-5P (Veefkind et al., 2012, Air Quality Expert Group, 2020, Wyche et al., 2021) and GOME on ESAs ERS-2 (Liu et al., 2005).~~(Molina and Molina, 2004)).~~ While these observations can provide global coverage extending over timescales of years, they generally contain limited information on the vertical distribution of pollutants within the column (Fleming, 1996, Peers et al., 2019). Instrumented aircraft provide one way of addressing this gap. Over several decades, there have been a number of related large-scale initiatives to instrument in-service commercial aircraft to provide such measurements, for example Measurements of OZone, water vapour, carbon monoxide and nitrogen oxides by Airbus In-service airCraft (MOZAIC, Solazzo et al., 2013) and In-service Aircraft for a Global Observing System (IAGOS, (Petzold et al., 2015)). Over forty-four thousand flights have been conducted under IAGOS since 1994 and though temporally and spatially restricted by commercial flight patterns and timings, these projects serve as a prime example of the use of instrumented aircraft to provide long term observations for atmospheric model evaluation. An alternative approach is the use of atmospheric research aircraft~~,~~ (ARA~~,),~~ which are ~~aircraft~~ instrumented and deployed specifically for the pursuit of atmospheric science and monitoring. ARA deployments tend to focus on specific locations or events and instrument payloads can vary greatly dependent on the phenomenon under study. As such, while ARA are particularly well suited to the detailed study of chemical and physical processes (a key requirement for model development), the often-sporadic nature of their deployment limits the generation of consistent, long-term datasets. It is this gap that this work seeks to fill with a specific focus on air quality observations over the UK to allow for the evaluation of regional models such as AQUM.

The UK Clean Air: Analysis and Solutions research programme is led by the Met Office and Natural Environment Research Council ~~(NERC)~~ and has invested in modelling, data and analytical tools to assess current and future air quality and the impact of policies designed to improve it (DEFRA, 2019). Under this umbrella, a long-term, quality assured dataset of the three-dimensional distribution of key pollutants (NO_2, O_3, SO_2 and $PM_{2.5}$) has been collected using the instrumented Met Office Atmospheric Survey Aircraft (MOASA). Observations have primarily covered the southern UK, including Greater London, with 63 flights throughout the period 2019-2022. This ~~sampling period encompasses~~ paper introduces the global COVID-19 pandemic lockdown, when emission of primary pollutants significantly reduced as a result of limits on mobility throughout the United Kingdom. As such the dataset may serve an additional application providing a unique resource with which to explore changes in atmospheric composition associated with reduced emissions during this period. This paper introduces the strategy and quality assurance basis for these observations and is not intended to be an in-depth diagnostic analysis, rather ~~strategy and quality assurance basis for these observations, with the intention of serving as~~ a comprehensive technical reference for all future users of these data, including illustrations of the potential uses of these upper air observations for regional-scale model evaluation.~~:~~ In particular it includes descriptions of~~:~~ i) the measurement platform and instrumentation, ii) flight strategies, iii) analysis of the spatial scales of measured pollutant variability, iv) ~~a comparison of ground-based observations to airborne observations from repeated flight patterns over Greater London and v)~~ initial use of these data to evaluate performance of the AQUM regional air quality model.~~, and v) an introduction to the vertical structure of pollutants observed during repeated flight patterns conducted over Greater London during the COVID-19 impacted period.~~

1.1 Impact of COVID-19

In January 2020, the first case of severe acute respiratory syndrome coronavirus (SARS-CoV-2), referred to as COVID-19, was identified in the UK (Jephcote et al., 2020). Since 24th March 2020, to curtail person-to-person transmission of the virus, the United Kingdom has been subject to various levels of lawful regulation limiting all non-essential travel and contact. A consequence of the restrictions has been a reduction in mobility (50-75% across major cities during the Spring 2020 lockdown, Air Quality Expert Group, 2020) as businesses switched to homeworking, and industry and commercial sectors reduced operations. This resulted in a significant drop in emissions of primary air pollutants, most markedly from the transport sector (road, rail, and aviation) and in urban environments. Similar impacts have been seen across Europe (Lee et al., 2020) and have collectively resulted in significant changes to UK air quality compared to the climatological norm (Air Quality Expert Group, 2020).

Flight operations with the MOASA aircraft encompass periods in 2020 and 2021 impacted by these COVID-related changes to air quality over the UK. The implications of this are two fold. Firstly, users of these data for model evaluation should be mindful that emissions throughout the measurement period were not always at climatological levels. In addition to bulk concentration changes, pollution properties such as particulate size and composition may also have been different during these periods. While this does not negate the use of these data for some aspects of model evaluation, it certainly cautions against their use to assess quantitative performance of models driven using standard climatological emissions. Secondly, and more positively from a scientific perspective, as the database includes observations covering pre , during and post lockdown periods, it presents a unique and valuable resource with which to further explore changes in atmospheric composition over the UK associated with reduced emissions during the COVID-19 impacted period.

2 MOASA capability

The MOASA, shown in figure 1, is a Cessna-421 aircraft based at Bournemouth airport, operated by Alto Aerospace Ltd for the Met Office .(Fig 1). The MOASA is instrumented to allow airborne measurement of key air quality-relevant aerosol and gas phase pollutants; namely gaseous nitrogen dioxide (NO_2), ozone (O_3), sulphur dioxide (SO_2), and fine mode aerosol ($PM_{2.5}$, determined indirectly from measurements of the aerosol size distribution). The fine mode aerosol is also characterised in terms of optical absorption and scattering properties. This section provides a detailed description of the MOASA instruments, which are summarised in table 1, and related quality assurance protocols.

2.1 Instrumentation – general setup

Instruments, examples of which can be seen in figure 2, are situated in the cabin, the front hold of the aircraft and under the wings. Wing-mounted probes include an Aircraft-Integrated Meteorological Measurement System (AIMMS, Aventech) instrument that provides real-time ambient meteorological data including temperature, humidity, pressure, three-dimensional winds (speed, direction, vertical) as well as latitude, longitude and (GPS) altitude. The aircraft also includes a wing-mounted Cloud, Aerosol and Precipitation Spectrometer with Particle-By-Particle (CAPS-PBP, Droplet Measurement Technology) (DMT)) though it does not form part of the air quality measurement suite and therefore is not discussed further here. Nitrogen dioxide, ozone and sulphur dioxide instruments are rack mounted in the cabin and sample at 0.85, 1.8 and 0.5 litres per minute, respectively. All instruments have a 1 Hz sampling resolution, except for the O_3 monitor which samples at 0.5 Hz. Ambient gaseous

samples are drawn from a stainless-steel air sample pipe that takes air from outside of the fuselage boundary layer through an on-rack PTFE headed sample pump (KNF N834.3FTE). Also within the cabin is a backscatter aerosol lidar (Leosphere) which is used operationally though does not form part of the core air quality measurement suite. The starboard side nose bay compartment contains a custom-built 'Air Quality Box' (AQ Box) and a nephelometer (Ecotech, Aurora 3000) (Fig 2). The sample to each of the instruments in the front hold is controlled with actuated valves and volume flow controllers inside the AQ Box (see ~~appendix~~Appendix A~~: for~~ AQ Box flow schematic).

The AQ Box contains a Portable Optical Particle Spectrometer (POPS, Handix) and a Tricolour Absorption Photometer (TAP, Brechtel, model 2901) and has the capability to sub-select only $PM_{2.5}$ sample aerosol for analysis. The sample into the AQ Box is from a Brechtel Iso-Kinetic inlet which samples at 6.35 litres per minute and has >95% sampling efficiency for particle diameters from 0.1 to 6 µm (Brechtel Manufacturing Inc, 2011). The $PM_{2.5}$ sample flow is dried via two Perma Pure MD-700 driers, connected in series via a 180-degree bend. The sample then passes through an impactor with an aerodynamic cut point size of 2.5 µm, before being split between the POPS (0.5 LPM (sample + sheath)), TAP (1 LPM) and the nephelometer (5 LPM) which is situated alongside the AQ Box. Measurements at the nephelometer and TAP inlet indicate the $PM_{2.5}$ sample relative humidity is typically below 20% and therefore the sample is a good representation of the dry $PM_{2.5}$ size distribution. Within the AQ Box the sample line temperature and pressure are also recorded.

Particle losses through the PM2.5 sampling lines have been estimated using open access particle loss calculation software (Von Der Weiden et al., 2009) based on the tubing dimensions, flow characteristics and a representative particle density of 1.64 gcm^{-3}. This analysis has suggested losses downstream of the inlet of <17% for particle diameters in the range 0.1 - 3µm.

In addition to particle losses due to flow deposition, we have considered the extent to which loss of particle mass may occur due to evaporation of ammonium nitrate, NH_4NO_3, a semi-volatile aerosol component that readily repartitions between condensed and gas phases upon changes in temperature and humidity (Nowak et al., 2010, Langridge et al., 2012, Morgan et al 2010). To determine the fractional loss of NH_4NO_3 during MOASA sampling, a kinetic model of the NH_4NO_3 evaporation process (based on the approach of Fuchs and Stutugin (1971), as implemented by Dassios and Pandis, 1999) was used to calculate the rate of change in diameter of polydisperse NH_4NO_3 particles through the MOASA flow system. The model unsurprisingly showed that the loss of particulate nitrate had a strong temperature dependence and varied dynamically as a function of time. Total mass losses during the MOASA sampling residence time of 2 seconds and at a representative sampling temperature of 30°C were approximately 7%. The NH_4NO_3 losses showed a weak dependence on pressure and relative humidity, with absolute losses increasing by only 2% at 500mb compared to 100mb and by approximately 2% over the relative humidity (RH) range 10-50% (where in-flight $PM_{2.5}$ sample RH was typically below 20%). Although evaporative loss of NH_4NO_3 during MOASA sampling will vary on a case-by-case basis, for representative conditions this work confirms that the loss is small and likely less than 7%.

The AQ box also allows for measurement of the aerosol population without particle size selection or drying, however this mode of operation has not been utilised in this work and is therefore not described further.

2.2 Nitrogen dioxide

A Cavity Attenuated Phase Shift Spectrometer Nitrogen Dioxide detector (Aerodyne Research Inc, referred to here as NO_2CAPS ~~to avoid confusion with the Cloud and Aerosol Precipitation Spectrometer, CAPS~~) was repackaged in-house, from a 5U, 12 kg to a 3U, 9.7 kg 19" rack-mounted unit to optimize volume and weight for airborne use. The analyser monitors ambient atmospheric NO_2 concentrations ~~„ with a lower detection limit of < 1~~ up to 3000 ppbv (parts per billion ~~(PPB),by volume)~~ using a 450 nm LED based absorption spectrometer utilizing cavity attenuated phase shift spectroscopy (Kebabian et al., 2005, Aerodyne Research, n.d.). A comprehensive review of the theory of operation is detailed in Kebabian et al., 2005. The NO_2CAPS analyser has been shown to be insensitive to other nitro-containing species and variability in ambient aerosol, humidity and other trace atmospheric species (Kebabian et al., 2005, Aerodyne Research, n.d.).

While some cavity-based absorption techniques are often referred to as calibration free (Langridge et al., 2008), this feature relies on knowledge of the variation in absorption cross-section across the spectral range of the light source being used. Given the broadband nature of the NO_2CAPS light source, which is difficult to characterise accurately and may be subject to change over time, we chose to undertake routine direct calibration of the instrument. As such, full multi-point calibrations are carried out annually at the National Centre for Atmospheric Science (NCAS) Atmospheric Measurement and Observation Facility (AMOF) COZI-lab at the University of York. Here, a multi-gas calibrator is used to dilute a high concentration NO standard into zero air (grade Pure Air Generator ~~(PAG)~~ 001) at varying levels. Ozone is added in excess to ensure full conversion of NO to NO_2. Seven concentration levels are used, and zero checks are also carried out. Calibration coefficients are determined from linear fits and applied to the NO_2CAPS during data post-processing.

2.2.1 NO_2 analyser baseline pressure dependency correction

During normal operation, the NO_2CAPS analyser periodically establishes a baseline to account for the optical losses associated with light transmission by the cavity mirrors (which depend both on mirror cleanliness and alignment) and Rayleigh scattering of light by air (Kebabian et al., 2005). This is achieved by passing NO_2 free air through the analyser every 15 minutes (automated). The standard NO_2CAPS software then applies a constant baseline correction based on these periodic measurements for the sampling segment that follows. For variable-pressure aircraft operation, this approach is not adequate as changes in Rayleigh scattering that accompany pressure changes lead to shifts in the instrument baseline between filter periods.

To account for these changes, a new correction scheme has been developed. During post processing, the pressure dependence of the baseline is determined by applying a linear fit to the pressure variation in Rayleigh-corrected filtered-air measurements recorded across the full flight. This dependence is used to calculate a new time-varying baseline based on sample pressure measurements alone. This baseline is then used to recalculate the NO_2 concentration across the flight. Spikes due to valve switches are also removed from the data series at this stage.

Figure 3 shows raw (red) and processed (blue) NO_2 concentration during flight M304 in November 2021, where the NO_2CAPS sample inlet was fitted with a zero-air filter such that measurements were sensitive only to baseline changes. Following take-off at 11:52:00 the aircraft climbed to an altitude of 5.5 km resulting in an ambient pressure change of 509 mb and a NO_2CAPS measurement-cell pressure change of 250 mb. The profile shows

corrected data is markedly more stable in comparison to the raw data and suggests a mean error in NO_2 concentration due to pressure-dependent baseline corrections of ± 0.09 ppbv (data averaged over 10s intervals). TheThe oscillations seen in the data during the filter test are an artefact of the filter, which impacted performance of the instrument pump. During a separate zero air test experiment, the sensitivity of the NO_2CAPS was empirically derived to be 0.17 ± 0.14σ ppbv (during a separate ground-based zero test, where data isdata also averaged over 10s intervals). As such, following correction, NO_2CAPS pressure sensitivity is not considered a significant source of uncertainty for aircraft NO_2CAPS observations.

2.3 Ozone

A dual beam ozone monitor (2B Tech, model 205) enables measurements of atmospheric ozone up to 100 ppmv (parts per million by volume). Measurements are based on the absorption of ultraviolet (UV) light at 254 nm in two absorption cells, one with ozone-scrubbed (zero) air and one with un-scrubbed (sample) air from which the Beer Lambert law can be used to determine ozone concentration. The instrumentInstrument sensitivity, empirically derived by sampling filtered air at 0.5 Hz during a test flight, is 2.9 ± 0.4 σ ppb. The monitor is calibrated annually at the NCAS AMOF COZI-lab where the instrument is compared with a NIST-traceable standard ozone spectrometer over a wide range of ozone mixing ratios. These results are used to calibrate the ozone monitor with respect to gain and sensitivity which are applied to the instrument directly.

A known but not widely recognized issue with UV absorption ozone monitors is that rapid changes in humidity (as may occur during airborne ascents and descents) can cause a large zero shift. This is due to modulation of humidity of the sample stream by the ozone scrubber which can cause the humidity in the sampling and zero cells to go out of equilibrium. To equilibrate the humidity, Nafion tubes known as DewLines are used in the 2B Tech monitor (Dewline, n.d., Wilson and Birks, 2006). Biases may become apparent should the DewLines stop working effectively and thus, following some initial issues with negative calculated ozone values during MOASA measurements (impacting the first 7 flights which do not have valid ozone data), the Dewlines were regularly replaced.

2.4 Sulphur dioxide

A pulsed florescence SO_2 analyser (Thermo Scientific, 43i Trace Level-Enhanced) detects sulphur dioxide up to 1000 ppbv. It operates on the principle that SO_2 molecules fluoresce following absorption of ultraviolet (UV) light, with the fluorescence intensity proportional to the number of SO_2 molecules in the air sample (Beecken et al., 2014). The instrumentInstrument sensitivity was empirically determined using zero-air checks to be 0.90 ± 0.26 σ ppb (averaged over 10s intervals). The SO_2 instrument is calibrated (zero and span) monthly in the field using an 863 ppb BOC Alpha Standard.

2.5 Aerosol scattering

A multi-wavelength integrating nephelometer (Ecotech, Aurora 3000) measures the light scattering coefficient of the aerosol population in both forward and back-scatter directions. It uses three high powered LED sources operating at wavelengths of 450, 525 and 635 nm.

Instrument sensitivity, determined from baseline statistics when sampling filtered air over 30 minutes at wavelengths 450, 525, and 635 nm was 0.05± 0.51σ, 0.10±0.55 σ and 0.01±0.69 σ Mm^{-1} for total scattering, and

0.21± 0.95 σ, 0.07± 0.49 σ and 0.14±0.55 σ Mm^{-1} for backscattering, respectively (data averaged over 10 s intervals). This falls within the manufacturer specified sensitivity of <0.3 Mm^{-1}. A monthly CO_2 calibration and annual in-house service are completed for the nephelometer as per manufacturer procedures (Ecotech, 2009).

Uncertainties in scattering measurements using the nephelometer are dependent on sample flow (empirically derived over all flights as < 0.05%), the uncertainty of calibration, inhomogeneities in Lambertian angular illumination, and truncation of light due to cell geometry. Corrections for angular truncation and non-Lambertian light source effects are applied according to the recommendations of Müller et al., 2011.

Müller et al., 2011 empirically calculated an uncertainty of 4% (450 nm), 2% (525 nm) and 5% (635 nm) for total scattering, and 7% (450 nm), 3% (525 nm) and 11% (635 nm) for total backscatter, which are adopted here. The signal to noise ratio for backscattering is worse compared to total scattering, since the backscattering signal is about one order of magnitude smaller than the total scattering signal for ambient air (Müller et al., 2011).

2.6 Aerosol absorption

Aerosol absorption is measured using a Tricolor Absorption Photometer (TAP, Brechtel, model 2901). The TAP is a 3-wavelength (467, 528, 652 nm) filter based absorption photometer which derives real-time aerosol light absorption from the difference in light transmission measured between two 47 mm diameter Pallflex (E70-2075W) glass-fibre filter spots, one of which receives particle laden air and the second of which receives aerosol-filtered air (Davies et al., 2019, Bond et al., 1999, Perim De Faria et al., 2021 and Ogren et al., 2017). The TAP employs empirical corrections to account for scattering effects that complicate the derivation of aerosol absorption from filter transmission measurements. The theory of operation and characterisation of the TAP is given in Ogren et al., 2017, Davies et al., 2019 (where it is previously known as a `CLAP').

Mean 1σ detection limits of the MOASA TAP, empirically derived by sampling filtered air and averaging over 60 seconds, are 0.22, 0.18 and 0.26 Mm^{-1} at wavelengths of 652, 528 and 467 nm, respectively. These values are in line with the manufacturer provided noise level characterisation of 0.20 Mm^{-1} over the same integration time.

The errors in absorption measurements from filter based photometry are dominated by uncertainties in the empirical scattering corrections, but also have contributions from uncertainties in the spectral response of the light source (±1-2 nm (Ogren et al., 2017)), sample flow rate (<1% (Ogren et al., 2017)), filter spot size and the penetration depth of particles within the filter matrix (Bond et al., 1999, Davies et al., 2019, Müller et al., 2014, Virkkula, 2010, Ogren et al., 2017). Internal particle losses within the instrument flow system due to diffusion, impaction and sedimentation are estimated to be < 1% for particles with diameters in the range 0.03–2.5 μm (Davies et al., 2019, Ogren et al., 2017). To minimise the effects of instrument noise observed in-flight, a low-pass filter is applied to raw data with a cut-off frequency of 0.08 Hz although this had minimal impact on optical properties derived from these data.

We apply scattering corrections to the low-pass-corrected TAP data using the Virkkula, 2010 correction scheme which relies on simultaneous measurements of the light scattering coefficient, which in this case are provided by the nephelometer. The correction scheme is implemented as described by Davies et al., 2019. Ogren et al., 2017 provided an estimate of the accuracy of TAP absorption measurements of 30% and this value is adopted here. However, as summarised by Davies et al., 2019, given the empirical nature of filter-based correction schemes and

strong source and wavelength dependencies, these correction schemes are unlikely to fully bound uncertainties associated with filter-based absorption measurements.

2.7 Aerosol size distributions

A portable optical particle counter (POPS, Handix) measures the size of dried particles predominantly in the accumulation mode (approximately 0.1 um < d < 1 um)(Haywood, 2008)using a light scattering technique. The POPS uses a spherical mirror to collect a fraction of light scattered sideways (38 – 142 degrees) by individual particles traversing a 405 nm laser beam. The scattered light is directed to a photomultiplier tube, the signal from which is digitised and placed into one of 32 bins that are spaced logarithmically in scattering amplitude space. For a given laser power, the measured scattering amplitude is determined by the particle size, shape, and index of refraction (IOR), thus allowing the bin boundaries to be converted to effective particle size subject to assumptions about shape and optical properties. In addition to particle size, given the POPS is a single particle instrument, it also provides a measure of the total particle number within its detection size range. A comprehensive review of POPS theory of operation is provided by Gao et al. (2016).

2.7.1 Calibration

Particle sizing by the POPS is calibrated by measuring the scattering amplitude of atomised NIST traceable polystyrene latex (PSL) spheres of known size, spherical shape and IOR (Rosenberg et al., 2012, Peers et al., 2019, Gao et al., 2016). Calibrations use 10 discrete sizes of PSL between 0.15 and 3 µm. The PSL are atomised and dried prior to entering the POPS sample inlet. PSL sizes between 0.15 and 0.70 µm are, where possible, also passed through a differential mobility analyser (~~DMA,~~ TSI 3082 Electrostatic Classifier) in order to help minimise the impacts of contaminants from the PSL generation process.

For each PSL diameter, Mie theory is used to calculate the particle scattering cross section (Fig 4), using a PSL IOR at 405nm of 1.615+0.001j (Gao et al., 2016). Linear regression is then used to fit the relationship between the POPS-measured scattering amplitude and the theoretical PSL scattering amplitude~~ (see Appendix B)~~ (Rosenberg et al., 2012)~~(Rosenberg et al., 2012)~~. The error in response is determined from the standard error in the mean for each 15 second period of sampling, averaged over the duration of the PSL run. The error in PSL diameter is the NIST-certified range of the PSL diameter. The linear regression function is used to assign calibrated scattering amplitudes to the designated POPS bin boundaries. At this point, the POPS measurements are calibrated.

To size ambient particles, it is necessary to convert the bin boundaries to equivalent diameters for particles with different optical properties. The impact of particle index of refraction on the POPS response is shown in figure~~Fig~~ 4 which shows the relationship between particle diameter and theoretical POPS response for both PSL's and particles representative of urban sampling. To account for the significant differences seen, we again apply Mie theory. The calibrated POPS bin boundaries in scattering cross section space are converted to diameter space based on Mie calculations. These calculations integrate scattering over the angular range of collection angles of the POPS and use an estimate of the ambient particle IOR (further details below) (Rosenberg et al., 2012, Gao et al., 2016). To overcome inherent Mie resonance oscillations in calculated scattering signals (where Dp > 600 nm in Fig 4), which result in non-monotonic behaviour with increasing particle diameter (van de Hulst 1981, Gao et al., 2016, Rosenberg et al., 2012), each Mie response curve is smoothed using spline interpolation (Hagan and

Kroll, 2020). As particle morphology and inter- and intra- particle homogeneity of the ambient sample are unknown, an assumption of spherical, homogeneous particles is implicit to the application of this Mie theory-based approach.

2.7.2 Index of Refraction

The IOR of the aerosol sample used for determination of POPS bins boundaries for ambient sampling is estimated using the method described in Liu and Daum, 2000 and Peers et al., 2019. This is an iterative approach whereby the single scattering albedo (the wavelength dependent ratio of aerosol scattering to total extinction, ω0) is calculated from the dry POPS particle size distribution ($\omega 0_{psd}$, λ = 405 nm) using an initial guess IOR and then compared to the measured single scattering albedo at 405 nm derived from independent observations from the MOASA nephelometer and TAP ($\omega 0_{nt}$). The IOR is then adjusted iteratively until acceptable closure is reached between calculated and measured ω0, noting that the POPS bin boundaries are adjusted upon each iteration.

This process is summarised in figure~~Fig~~ 5 and more detail, including a case study, is in appendix B: Index of refraction corrections~~Appendix 5~~.

A strength of the MOASA data set is that the POPS, TAP and nephelometer all share a common sample inlet, which reduces the potential source of sampling bias that may impact this analysis. Further, to minimise differences in sampling volumes and response times, all ω0 calculations are performed using 30 second averaged data and only data from straight and level runs (SLR, flight transects at approximate constant altitude and velocity) of at least 3 minutes duration are included. The iterative IOR analysis step is performed on the flight-mean of these SLR data. While this approach does not allow in-flight variability to be accounted for, it minimises potential for erroneous impacts on the POPS size distribution arising from noise and uncertainty in the ω0 measurements, which can be large at low aerosol loading levels. The flight-average approach adopted here has been shown to lead to modest errors in particle diameter of <10% compared to analysis at finer temporal scales (see ~~Appendix C,~~ case study ~~in Appendix C~~). We also note while the IOR derived here provides closure between MOASA optical ~~and size distribution~~ instruments, it is subject to potential uncertainties~~, such as assumptions of aerosol homogeneity and sphericity,~~ that caution against its use as an accurate measure of the true ambient particle IOR (Frie and Bahreini, 2021)~~.~~.

2.7.3 Size distribution uncertainties

A review of uncertainties for the POPS instrument is given in Gao et al. (2016). For particle number measurements, the main source of uncertainty for particles within the instrument's size detection range is the sample flow rate. Gao et al. (2016) report a nominal sample flow rate of 3 cm^3 s^{-1} with an upper limit of 6.67 cm^3 s^{-1} and associated error of <10 % (personal communication, Handix, October 2020). For the MOASA POPS the sample flow over all flights ranged from 2.7 to 5.9 cm^3 s^{-1} (data averaged over 10s intervals). The higher values arose due to flow system cross-interference issues that generated flow noise impacting the first 11 MOASA flights, following which the source of noise was removed and a more representative range of normal operation is 2.9 cm^3 s^{-1} ± 3.2%.

Coincidence errors, whereby two or more particles traverse the laser beam at the same time leading to sizing errors, are a common feature of all optical particle counters when used in high aerosol loading environments. The

impact of coincidence errors on the MOASA POPS observations are addressed during data processing by flagging all data where particle concentrations exceed 7000 cm^3/s (McMeeking, 2020, personal communication).

Particle sizing uncertainties arise from a number of sources, including scattering amplitude measurement uncertainty (leading to an estimated 3% 1σ sizing error for 500 nm particles) and laser intensity instability (±3 % diameter sizing error for temperatures from 43 to 46 ºC). In addition, for reasons already discussed above, uncertainty in the IOR of particles being measured also impact uncertainty in particle sizing. Gao et al. (2016) used a theoretical ambient aerosol population to investigate the potential magnitude of this error. They assessed the accuracy in the location and width of lognormal fits to both a theoretical population fine mode (10% and 10% respectively) and coarse mode (1.4% and 19% respectively). These uncertainties were propagated to derive an estimated uncertainty in the total particle volume of 19%. Though based on a single theoretical ambient size distribution, this analysis provides an indication of the magnitude of error arising from IOR variation. For MOASA POPS-derived size distributions, it is likely to provide an upper indication of the error, given that efforts to correct the POPS bin boundaries based on the iterative IOR method described above should serve to improve sizing accuracy.

Based on the information above, an upper estimate for the error in total particle volume from POPS measurements (required for subsequent calculation of particle mass) is derived by combining in quadrature contributions from IOR/scattering (19%), sample flow (3.2%) and laser amplitude (6%) to yield an uncertainty of 20%.

2.8 Determination of mass concentration (PM2.5)

To calculate particulate mass, we convert the calibrated, IOR-corrected POPS particle size distributions to volume distributions, and subsequently mass distributions by assuming a fixed particle density. The total mass is then calculated by integrating across the distribution within the $PM_{2.5}$ size range. Calculations are performed on 10 second averaged data and work on the basis of fitting lognormal functions to the measured distributions to represent a fine and coarse mode (the dashed line in figure~~Fig~~ 6 show~~shows~~ the combined lognormal modes from a straight and level run during flight M270 on 15th September 2020). This approach serves to reduce the impact of residual structure from Mie resonances in the POPS distribution on mass derivations.

The selection of an appropriate particle density for converting volume to mass is an important part of the above analysis. The composition and therefore density of ambient aerosol varies dynamically in the atmosphere (Wang et al., 2009, Crilley et al., 2020). In the absence of co-located aerosol composition observations on MOASA, we apply a fixed density to all data of 1.64 ± 0.07 (1σ) gcm^3. This value is derived by weight-averaging the densities of $PM_{2.5}$ aerosol components measured during a range of UK field experiments, as detailed in appendix C~~Appendix D~~.

The total uncertainty in the determined $PM_{2.5}$ mass concentration, estimated by combining uncertainties in the measured particle volume (20%) and the assumed particle density (4.2%), is 20.4% and thus dominated by the volume error.

3 Flight Planning

The MOASA air quality flight strategy was based on flying a series of repeated sorties, each designed to provide data suitable for different aspects of model evaluation work. On a week-to-week basis, sorties were selected based on the prevailing weather conditions and any required modifications to flight plans ~~were~~are made at that time. This section describes the rationale behind each of the sortie types, together with a summary of flight activities.

Given the MOASA home base is at Bournemouth on the south coast of the UK, operations have predominantly focused on sampling over the south of the UK. This includes work over the English Channel (e.g., sampling transboundary pollution), over varied land-use types (urban and rural) including pollution hotspots such as London, and over isolated source regions such as docks and industrial sites. In addition to regular sorties, in June/~~and~~ July 2021 ~~(summer) and January/March 2022 (winter),~~ the MOASA also participated in ~~an~~ Intensive Observation ~~Periods (IOP's~~Period (IOP) in conjunction with ground based ~~Integrated Research Observation System for Clean Air (OSCA)~~ air quality super-sites~~,~~ located in London, Birmingham and Manchester (UKRI, 2021, OSCA, 2020). All flights are performed within operational airspace regulations which limit minimum and maximum flight levels. Observations are mostly in the boundary layer and, as shown in Fig ~~7, bottom panel~~8, typically near or below 1 km GPS altitude. The lowest altitudes (0.15 km minimum) are permitted in offshore and rural areas, whereas minimum altitudes in urban areas (or in regions with significant topography or obstacles like masts or chimneys) are limited to > 0.3 km. Where possible profile measurements extending into the free troposphere are also collected, which allow the boundary layer height to be determined in addition to sampling of aged and/or transported pollutants.

In terms of meteorology, conditions representative of both the general background environment and elevated pollution events have been targeted. As the southern UK has a maritime climate, with the frequent passage of mobile low-pressure systems from the North Atlantic, conditions in the operating area are not always conducive to the build-up of pollution. For the targeting of elevated pollution conditions, synoptic high-pressure conditions with light winds and little cloud/precipitation are favoured. Strong sunshine and elevated temperatures are also conducive to the production and build-up of pollutants such as ozone and as such, high pollution events tend to be more frequent and severe in the summer (Savage et al., 2013).

3.1 Ground Network Survey

Ground Network Survey sorties describe two flight patterns that sample both rural and urban background regional pollution at various altitudes. One flight pattern is focused on the southwestern UK (Fig ~~8~~7, panel A1) and the other on the eastern UK (Fig ~~8~~7.A2). A particular feature of these sorties is that they overfly a number of AURN ground sites allowing pollutant concentrations at the surface to be compared to those aloft. Characterisation of pollution at regional scales is important for air quality model evaluation, particularly for models operating at coarse resolutions such as AQUM, which encompass point-source emissions data but cannot accurately represent them in terms of location and concentration.

3.2 High-Density Plume Mapping

High Density Plume Mapping flights (Fig ~~8~~7.B) use intensive model grid-box scale sampling to allow for assessment of the (often sub-grid in models) scale of pollutant variability in a high pollution region. Repeated

runs upwind, downwind and within the plume are performed at a range of altitudes. This sortie has primarily been flown over Port Talbot in South Wales, a heavily industrialised area and AQUM pollution hotspot, but has also been flown once north of Cambridge (east UK). In that case, horizontal transects sampling the plume at multiple altitudes downwind of the city were conducted.

3.3 South Coast Survey

South Coast Surveys were flown onshore and offshore along the south coast of the UK, typically from Dartmoor National Park in the western UK to Eastbourne in the east (Fig ~~8~~7.C). These surveys have been flown under background and polluted southerly flows to characterise transboundary and long-range transport of pollutants from continental Europe. In late 2019, a persistent emissions hot spot (primarily $PM_{2.5}$ and SO_2) was seen in the AQUM forecasts, potentially originating from ships in Southampton Docks. Therefore, from late 2019 onwards, overflights of the Solent and Southampton Waters were added to the stock sortie.

3.4 Coastal Transition Survey

The coastal transition sortie (Fig ~~8~~7.D) also operates along the south coast of the UK. The primary distinction from the south coast survey was a zigzag manoeuvre whereby observations across the land-to-sea transition are repeatedly sampled. The objective for this sortie is to obtain data for benchmarking model performance across the land-sea interface where strong gradients in humidity and temperature can impact forecast pollution fields. In later flights, these surveys have also been extended eastwards to encompass the Dover Straights to allow sampling of pollutants transported from industrial activities around the Dunkirk region of northern France, which is another emissions hotspot that can lead to strong pollutant transport over the UK when meteorological conditions permit.

3.5 London City Survey

Circumnavigational flights of London (Fig ~~8~~7.E) were performed during high and low pollutant loadings to characterise city scale emission and dispersion of pollutants from the heavily populated, commercial, and industrial Greater London area. Busy air space and air traffic control due to the close proximity to major airports (Gatwick, London City, Heathrow) restrict the operational area of the MOASA. Broadly, following a short transit to Reading, the sortie takes the MOASA clockwise following the M25 London orbital motorway, which encircles Greater London. Missed approaches are frequently performed at Elstree airfield to the north and Biggin Hill airfield to the southeast.

A substantial decrease in air traffic during the COVID-19 pandemic provided a unique opportunity to fly at low level (approx. 1000 ft) over central London. This central city sampling was added to the stock sortie in November 2020 and became the primary sortie for flights during the COVID-19 pandemic. The central London overpass follows the Thames River to approximately 0.087°W where it deviates south-westerly to comply with air traffic control restrictions. During later flights, north-south and/or east-west transects were also completed to observe the urban heat island effect on boundary layer height. During the summer~~IOP's in June-July 2021,~~ and winter IOP's~~January-February 2022~~ MOASA observations were also made close to the surface air-quality IOP supersite (stars, Fig ~~8~~7.E).

3.6 Birmingham and Manchester IOP

During the summer and winter ~~Clean Air ground based~~ IOP's ~~in June-July 2021, and January-March 2022~~ MOASA observations were also made over Birmingham (Fig ~~8~~7.F) and Manchester (Fig ~~8~~7.G). These city scale sorties were tailored to best suit meteorological conditions on the flight day, and typically involved circumnavigational orbits, or box patterns over the cities at altitudes ranging from approximately 0.3 to 0.9 km and/or runs north to south, up wind and downwind of the city and supersite. Passes directly overhead of the Birmingham and Manchester ground supersites (stars, Fig ~~8f~~7f and ~~8g~~7g) were made at each altitude, when possible. During the IOP, MOASA operated both in the morning and late afternoon, allowing observation of the build-up of regional scale pollutants over the day. Further MOASA flights in these regions are anticipated during a second ground based IOP planned for winter 2021/22.

3.7 Summary

63 flight sorties were flown between ~~July~~June 2019 to April 2022, comprising over 150 hours of atmospheric sampling. Flight details are summarised in table 2 and figure 7~~1. Figure 8~~ shows horizontal and vertical spatial coverage of flights over the Clean Air campaign.

3.8 The MOASA measurement database

Datasets obtained during the MOASA Clean Air project are openly available from the Centre for Environmental Data Archive (CEDA) "Collection of airborne atmospheric measurements for the MOASA Clean Air project" repository (DOI: 10.5285/0aa1ec0cf18e4065bdae8ae39260fe7d).

Data files are NetCDF format and contain observations from the NO_2CAPS (NO_2, ppbv, 1Hz), Ozone monitor (O_3, 0.5 Hz, ppbv), SO_2 analyser (SO_2, ppbv, 1Hz), nephelometer (light scattering, Mm^{-1}, 1 Hz), TAP (light absorption, Mm^{-1}, 1Hz), POPS (particle counts, and calibrated, IOR corrected particle concentration, total mass ($\mu g\ m^{-3}$ / bin) and $PM_{2.5}$ ($\mu g\ m^{-3}$), 1 Hz), as well as meteorological parameters observed by the AIMMS-20 (ambient temperature (^oC), relative humidity (%), pressure (hPa) and wind speed (m/s) and wind direction (degree), 1 Hz). Each instrument parameter is presented as a time synchronised, three-dimensionally geo-located time-series, with calibrations and corrections applied (where applicable). Each instrument parameter has a standard name, long name, unit and measurement frequency (compliant with Climate and Forecast (CF) naming conventions where possible)~~,.), which are listed in Appendix 7.~~ Some, but not all, also have a comment, minimum and maximum limits and/or a positive attribute. Each variable has the coordinates of time, latitude, longitude and altitude. Measurements from all instruments are reported at ambient pressure and temperature.

To ensure optimal traceability and transparency of data, comprehensive metadata is included in the NetCDF which details any calibration constants and/or corrections applied to data alongside general information about the data, such as contacts, acronyms and references. ~~Where possible, data~~Data is range checked to ensure observations fall inside the recommended operational limits of the instrument and outliers to these limits are flagged. The standard flag name~~format~~ is the parameter name, post fixed with '_flag'. The three flag values are: 0 = good_data, 1 = outside_valid_ranges, and 2 = sensor_nonfunctional. ~~Where a~~For flag ~~is available, =~~1, the valid ranges are given in the variable metadata. Each flag parameter has standard name, frequency, flag value and flag meaning attributes. ~~Housekeeping variable flags are carried forward to the primary~~Derived variables~~, primary variable~~

~~flags are carried forward to secondary variables.~~ (for example, $PM_{2.5}$ or Angstrom exponents) do not have flags. The configuration file used to process each flight data is available alongside the NetCDF as a text file and provides the range check limits and the source of these limits. Records of all work done on the instruments (calibrations, cleaning, and maintenance) are digitally recorded and available on request ~~by contacting the author~~.

4 Flight data examples

This section provides a limited number of case studies applying the MOASA dataset to different scientific applications. These examples are intended to showcase different uses of the database and are not intended as comprehensive analyses in their own right. We present: i) a statistical analysis of the scales of pollutant variability observed across the MOASA air quality dataset, ii) ~~an introduction to the vertical structure of pollutants by comparing ground-based observations to airborne observations from repeated flight patterns over Greater London and iii)~~ example use of the dataset for evaluation of a regional air quality modelling system (AQUM).~~), and iii) the vertical structure of pollutants observed during repeated flight patterns over Greater London, including during the COVID-19 impacted period.~~

4.1 The spatial scales of pollutant variability

The evaluation of limited-resolution regional air quality models (such as AQUM with a 12km grid length) using high resolution in-situ surface or airborne data, is complicated by the differences in spatial scale between the two (Qian et al., 2010). While instrumentation may be capable of measurements at high precision and accuracy, these uncertainty metrics often don't determine the degree to which models and observations should be expected to agree. In many cases the magnitude of natural pollutant variability at scales that are sub-grid for models provides an important additional consideration. Quantifying sub-grid scale pollutant variability is also important for wider applications beyond model evaluation, such as pollutant exposure studies (e.g. Denby et al., 2011) and in understanding satellite-derived data (e.g. Tang et al., 2021). With this in mind, in this section we use the MOASA Clean Air database to assess how observed pollutant variability changes, on average, as a function of length scale, and how this variability compares to fundamental instrument measurement precision. As with each analysis presented in this section, the intention is to provide insight into potential application areas for the MOASA dataset, rather than provide a comprehensive study.

~~The evaluation of limited-resolution regional air quality models (such as AQUM with a 12km grid length) using high resolution in-situ surface or airborne data, is complicated by the differences in spatial scale between the two. While instrumentation may be capable of measurements at high precision and accuracy, these uncertainty metrics may, or may not, provide criteria suitable for determining the degree to which models and observations should agree. In many cases the magnitude of natural pollutant variability at scales that are sub-grid for models provides an important additional consideration. With this in mind, in this section we use the MOASA Clean Air database to assess how observed pollutant variability changes, on average, as a function of length scale, and how this variability compares to fundamental instrument measurement precision.~~

~~We take a statistical approach that uses data from all MOASA SLRs, over 44 flights between July 2019 and July 2021. The number of SLRs per flight varies depending on the type of sortie flown, with a minimum of 2 and a maximum of 11 (see table 1). The minimum permissible SLR length was capped at 3 minutes to ensure adequate~~

~~counting statistics. In total this yielded 240 SLRs representing 1,389 minutes of sampling and we focus here on measurements of relative humidity, NO_2, SO_2 and total particle number concentration.~~

High temporal resolution datasets corresponding to each straight and level run ~~(e.g., SO_2 in Fig 9),~~ formed the basis for the analysis. An example straight and level run is shown in figure 9, which, notably, shows that SO_2 data was generally below the sensitivity of the instrument except during exceedance events. Measured values in each dataset were split into groups of equal size, with sizes corresponding to equivalent ground distances (d_{int}) ranging from 0.42 km to 17 km, in 0.085 km (1 second) intervals (where a true airspeed of 85 m/s is assumed to be equivalent to 0.085 km per second straight-line distance at ground level).~~.~~ The variability observed at each of these length scales was calculated by first calculating the standard deviation (σ) of points within each group of data, before calculating the mean deviation across all groups in the transect.

The variability observed in a given transect depends on a range of factors and will clearly change on a case-by-case basis. Despite this, it is also useful to examine how, an average, sub grid variability changes as a function of length scale (e.g. Tang et al., 2021 and references therein). This has been investigated here by using averaging data from all MOASA SLRs, over 63 flights between July 2019 to April 2022 (322 SLRs representing 1,952 minutes of sampling). The number of SLRs per flight varies depending on the type of sortie flown, with a minimum of 2 and a maximum of 11 (see table 2). The minimum permissible SLR length was capped at 3 minutes to ensure adequate counting statistics. We focus here on measurements of relative humidity, NO_2, SO_2 and total particle number concentration. The results are presented in figure 10 as probability density functions that indicate the range of variability observed at~~In order to provide a more statistically robust indication of ambient variability than possible from a single transect, the mean transect σ for each d_{int} was averaged across all flight transects to give the flight mean variability (e.g., Fig 10 for flight M284). Further, the analysis was extended to all flights in the MOASA database, with results presented in Fig 11 as probability density functions of the mean transect σ at selected~~ d_{int} of 0.42, 0.85, 2.55, 5.10, 12.07, and 15.04 km.

Of particular note, it is clear that measured variability in SO_2 was generally close to or below the noise limit of the MOASA instrumentation, thus instrument performance dominates not only SO_2 data (as seen in Fig 9) but also observed SO_2 variability in the MOASA database. For RH, NO_2 and particle counts, natural variability is generally well sampled by the MOASA instrumentation. It is interesting to note how the peak position and width of the distributions changes upon moving to progressively longer sampling scales. Changes are particularly marked for relative humidity and somewhat less so for NO_2 and particulate counts. Focusing on the 12km AQUM grid length as an example, >99 % of NO_2 variability observed over the campaign is above instrument noise. This indicates that a significant amount of the variability in the NO_2 dataset can be interpreted as natural/real pollutant variability that could be used to help bound model parameterisations of sub-grid variability, evaluate the accuracy of exposure estimates in air quality models, as discussed in Denby et al., 2011 and facilitate estimations of sampling uncertainties for satellite product validation, which has historically been limited by availability of such in-situ measurements (Tang et al., 2021) .

~~Figure 10 shows that the variability in observed RH, SO_2, NO_2 and particulate counts increased as a function of sampling scale. This result is unsurprising given that natural variability can only increase when observing over greater spatial scales. Interestingly the increase is non-linear, showing rapid change over scales of 0.5-2 km before~~

~~levelling at scales towards 15 km. For reference, the AQUM grid length of 12km is marked on the plots (vertical dotted line). The horizontal dashed red lines on Fig 10 show the precision of measurements derived from ground-based zero tests (where available) where SO_2 = 0.90 ± 0.26 σ ppbv, particle counts = 2.95 ± 0.74 σ counts and NO_2 = 0.17 ppbv ± 0.14. It is clear that even at the smallest spatial scale of 0.42 km, instrument precision did not limit ability to sample the natural pollutant variability for this flight.~~

~~.~~4.2 Ground-based and airborne observation comparison using long term observations over London

To enable meaningful comparison of airborne and ground-based observations during model verification, the relationship between observation methods must first be understood. To achieve this understanding, in this section, a comparison of airborne and ground-based observational data is presented.

The ground-based observations consist of OSCA mast and AURN data. AURN consists of around 70 sites in rural, remote, urban background and suburban settings, providing hourly measurements of NO_x, SO_2, O_3, carbon monoxide (CO), $PM_{2.5}$ and coarse particulate matter (PM_{10}) (Yardley et al., 2012), although not all species are measured at all sites. For this paper, we only consider background AURN sites applicable to regional air quality models such as AQUM (Neal et al., 2014)~~.~~

For the comparison, first, the vertical structure of NO_2, $PM_{2.5}$, SO_2 and O_3 were plotted as altitude profiles of airborne data alongside all available ground data within Greater London (longitudes from -0.60 to 0.40, latitudes from 51.23 to 51.80). The agreement (ratio) between airborne and ground-based observations was moderately low for all species for most flights, likely due to large variation between ground sites, in terms of site proximity to the airborne data and variation in concentration due to proximity to emission sources. An example of the vertical and horizonal spatial variation of airborne and ground-based observations for NO_2 during flight M325 over Greater London is shown in figure 11~~14~~. Here, the HIL AURN site, observed at 84 μgm^3 (fig 11~~14~~ left: grey square and right: red triangle) is significantly higher than both other ground-sites in the region and the range of airborne data (boxplot whiskers in fig 11~~fig14~~ left, and track colour in fig 11~~figure 14~~, right). This skews the airborne:ground ratio to 0.32 (the ratio discounting this site is 0.48). This suggests region-wide observational comparison is insufficient in determining if the airborne data can be meaningfully compared to the ground data and is an inefficient metric when using these observations for model evaluation, where models can have significantly higher resolution. As shown in sec. 4.1, MOASA instrument precision did not limit the ability to sample the natural pollutant variability at spatial scales of 0.42 km, important for representing the magnitude of natural pollutant variability at scales that are sub-grid for models.

To minimise the effects of the horizontal spatial variation of concentrations and utilise the high spatial resolution of the airborne data, the average airborne observation within a 12 km radius (the AQUM grid length) of each ground site was calculated. For each species, these airborne averages were plotted against the local ground-based average observation, for each ground site, for each IOP flight. Linear regression was then modelled for each species and site. The result of this approach is shown in figure 12~~15~~ for the Greater London area.

4.2.1 $PM_{2.5}$

Linear regression of airborne vs ground-based observations of $PM_{2.5}$ inside the London area suggests very good agreement between the two datasets, with r^2 of 0.90. The agreement between observations suggests a well-mixed atmosphere, with little gradient in $PM_{2.5}$ throughout the column. The majority of observations are obtained using the same measurement technique (optical particle counter with conversion to mass concentration) with just one AURN site (London Westminster) using a beta-ray attenuation (BRA) technique. As discussed in section 2.8, airborne $PM_{2.5}$ is derived from size distributions that are refractive index corrected on a per-flight basis, and a density of 1.64 g/cm^3. For the majority of AURN ground sites, both refractive index and density are derived internally to the instrument, using 24 hr average gravimetric data. This comparison suggests these correction methods yield agreeable results. The parity of the BRA observations with the majority equivalent method provides further reassurance that, for this study, all observations of $PM_{2.5}$ are comparable, regardless of observation technique employed.

4.2.2 SO_2

Due to limited AURN sites that observe SO_2, and low concentrations of SO_2 which generally do not exceed the uncertainty thresholds of the airborne instrumentation, there are insufficient observations to explore agreement between the observational platforms, which both employ a UV fluorescence technique. However, at the low concentrations shown and the site data available, the observations show reasonable agreement. That both airborne and ground-based observations are made using the same measurement technique provides further confidence that the observations are comparable.

4.2.3 NO_2 and O_3

A weaker positive, agreement is shown for NO_2 where $r^2 = 0.40$, suggesting a more variable relationship between airborne and ground-based observations. The model slope of 0.12 predicts systematically lower NO_2 observations aloft at most sites, which diverge further away from unison with increase in concentration.

A moderate, positive agreement is seen for O_3, where $r^2 = 0.63$. The regression model predicts systemically higher observations aloft at all sites, and the model gradient of 0.48 approaches unison towards higher concentrations, contrary to the NO_2 model. Flight dates for observations at lower O_3 concentration were in winter, whereas flight dates for observations of the highest concentrations – where agreement is strongest - are in the summer/spring months.

All observations of O_3 use ultraviolet photometry, whereas, for NO_2, observations aloft and at the OSCA mast sites use cavity attenuated phase shift spectroscopy, and the AURN sites employ a chemiluminescence. There are numerous possible explanations as to why we might not expect observations at the ground and aloft to agree well for these reactive chemical species, including instrument bias (particularly for NO_2 which employs different observation techniques) and complex chemistry throughout the column.

Assuming the simplest chemical setup, whereby chemistry in the vertical is controlled by O_3 titration ($O_3 + NO_2 \Rightarrow NO$), odd oxygen ($O_x$, a chemical family comprised of the sum of all gas-and particulate-phase species which contain an odd oxygen (atoms or ozone) (Womack et al., 2019, Bates and Jacob, 2019)) is expected to be conserved throughout the atmospheric profile. Figure 13~~16~~ shows O_x~~odd oxygen~~ (calculated by summing the

average airborne and average ground based O_3 and NO_2 on a molecular level (PPB), for each flight that had both species~~O3 and NO2~~ available), for the London site yields a regression model gradient of near 1, with higher concentrations aloft. These results are broadly consistent with chemistry via O_3 titration being dominant and indicate that the airborne air masses were coupled to the surface, conducive to the findings of the $PM_{2.5}$ analysis. An r^2 of 0.87 also provides confidence that the observations are comparable, regardless of observation technique employed.

4.2.4 Summary

The overall strong correlation between airborne and ground based $PM_{2.5}$ implies the observations are likely comparable when made within a well-mixed boundary layer. The low sample, low concentration SO_2 observations analysed here also suggest the observations are comparable. For NO_2 and O_3, complex chemistry in the atmospheric column yields an intricate relationship between airborne and ground-based observations. Analysis of odd oxygen implies O_3 titration is the dominant throughout the column, although a slight offset, suggesting O_3 is higher aloft, remains, suggesting ~~a~~ processes unrepresented by this model may be present. Overall, these results suggest there is no fundamental issue in using the high-horizontally spatial resolution airborne observations in model comparison, to substantially augment the sparse ground observations in model analysis, and to further explore these complex chemical processes in the horizontal and vertical, and how they are represented in models.

4.3 Preliminary model evaluation

In this section we show examples from two flights illustrating how the MOASA Clean Air database can be used for model evaluation purposes. These flights are: M270 high density plume mapping on 15th September 2020, selected to measure the vertical distribution of pollutants in the lower atmosphere north of Cambridge (52.2053° N, 0.1218° E) and M296, a Birmingham city survey as part of the IOP on 1st July 2021. Meteorological conditions for the flights are summarised in figure 14~~Fig 12~~. For M270, there were largely clear skies with light winds (<10 m/s) in the south east UK where sampling was undertaken, and high temperatures (The National Meteorological Library, 2020), conducive to the accumulation of pollutants in the boundary layer. M296 was influenced by high pressure, light winds and thin broken cloud.

Case studies of the flight days have been run using the AQUM UK domain model. This is the same model configuration used for the operational air quality forecasting, but for these case studies, no ~~routine~~ statistical post-processing (SPP, which uses surface level observations to apply corrections to the surface model level only) has been applied to the data. Given this study focuses on those data above the surface level, the omission of the SSP has no impact on the evaluation. Each simulation has been run with a 7 day spin up period. No adjustments have been made to the emissions used by the model to account for changes in activities during the COVID-19 restrictions. Model data points have been linearly interpolated using the time, latitude, longitude and altitude coordinates of the aircraft at 1 second frequency. The model and aircraft data along the flight tracks have then been averaged into 10 second, non-overlapping intervals.

4.3.1 ~~*** THE BELOW HAS BEEN SIGNIFICANTLY RESCTRUCTURED***~~

Flight M270

In consonance with Savage et al. (2013), who, as discussed in sec. 1, reported positive model ozone biases during a ground-site AQUM comparison,, a large ozone bias is seen for flight M270 (Fig 1516.a). The model data show large overprediction when compared against the aircraft data at corresponding locations (mean model bias of 18.49 ppb). The bias is lowest near to the surface and increases with altitude up to approximately 700 - 800 m, above which the bias decreases. The variability observedIt is poorly represented by the coarse resolutionof note that the observations are more variable than the model, at all altitudes, which is due to the relatively short flight track in the context of the 12 km model. Variation in the AQUM model data is largely caused by changing from one grid box to the other and ozone shows a typically smooth gradient between model grid boxes. We note that in this case the stacked flight transects only crossHence a very small number of model cells (3 or 4) in the horizontal, which may be accountable for the lowflight track which crosses fewer grid boxes will show relatively lower model variability seen here.compared to the observational data, which as discussed in sec 4.1, represents smaller scale natural variability. Figure 1617 shows the comparison between the model and aircraft NO_2 data for vertically stacked transects for the same time periodtransect. The agreement is generally good (within ± 2 ppbv) below 650 m altitude, but the model shows large under-prediction above this altitude. Temperature and relative humidity profiles measured by the aircraft (not shown) suggests a boundary layer height of approximately 1100 m on this day, which corresponds with a decrease in observed NO_2 concentration above this height. However, the average boundary layer height in the model for the observed area is approximately 620 m. This indicates a potential under-prediction in boundary layer height that may be responsible for the poor predication of NO_2 at elevated altitudes and elucidates the altitude dependence on the ozone model bias discussed above.

4.3.2 Flight M296

A large positive model ozone bias is also seen for flight M296 (Fig 1516.b) when compared against the aircraft data at corresponding locations (mean model bias of 48.93 ppb). Unlike flight M270, the bias appears relatively constant with altitude, likely due to the flight being solely inside the boundary layer. Also unlike flight M270, the observations and model show similar variability. This is likely, due to the flight track crossing a larger number of model cells which encompassarea and thus encompassing more model predictions,grid boxes and may also be due toincreasing the amount of variation seen in the model capturing more variability for this casedata.

Figure 1718 shows model and observed NO_2 concentration throughout the first and fourth stacked box patterns performed around Birmingham during M296. Strong variation is observed in NO_2 concentration aloft of the city, including enhanced NO_2 at all altitudes (maximum 55.70, 49.44, 56.31 and 54.06 µg/m^3 NO_2 for circuits 1-4, respectively. See appendix DE for circuits 2 and 3-). The enhanced NO_2 plume is seen above the western quadrant of the city during the lowest altitude circuit (circuit 1, 423 m, 11:23 to 11:43 UTC) and moves southeast with increasing altitude, until the plume is observed primarily over the southeast quadrant of the city during the highest altitude circuit (circuit 4, 657 m, 12:33 to 12:52). As expected, given that NO_2 is photochemically split during the formation of O_3, observed O_3ozone aloft (not shown) is inverse to the variable NO_2 observations, and shows a reduction of approx. 20-30 µgm^3 at the plume locations at all altitudes. around the flight track. Comparison of NO_2 aloft with average surface-level observations over the transect time (triangles, 1 hour data frequency) show similar concentrations. In consonance with AQUM, light north-westerly winds (0 < 5 knots) associated with the high-pressure system are observed in all circuits. These slack winds (equivalent to a maximum velocity south-

~~eastward at 9.26 km per hour) likely~~may have pushed the ~~plume (which is seen in the ground data to be present east of the flight track)~~airmass south-eastward, accounting for the shift in the ~~observed~~ plume with altitude and time (approximately 1 hour between the first and final circuits). The proximity of the plume to Birmingham airport is also of note in run 4.~~.~~ The AQUM model shows little variation and low NO_2 concentration in comparison to both airborne and ground-based observations in all circuits above the city (maximum 14.44, 13.91, 11.43 and 10.33 ug/m^3 NO_2 for circuits 1-4, respectively, which decrease imperceptibly with altitude). A negative NO_2 model bias is evident at the observed plume locations, with maximum differences of -44.26, -44.30, -49.22 and -49.79 ug/m^3 NO_2 for circuits 1-4, respectively. This model bias is expected to have been larger if the AQUM data was produced using emissions modified for the COVID-19 pandemic (Grange et al., 2021).

Given the flight track is mostly within just four model grid boxes, variation in NO_2 concentration from point source emissions is not expected to be represented in fine detail in the model. As the observed peak in NO_2 is located downwind of important sources (motorways and a heavily urbanised area), and , given the dependence of surface concentrations of this primary pollutant on local emissions (Neal et al., 2017) the lack of enhanced NO_2 at all levels of the model could be attributed to emissions being too low at the observed plume location.~~Given the aircraft flight track is mostly within just four model grid boxes, variation in NO_2 concentration from point source emissions is not expected to be represented in fine detail in the model. Given the observed peak in NO_2 is located downwind of important sources (motorways and a heavily urbanised area), and model winds agree well with the observed winds, the lack of any enhanced NO_2 at all levels of the model could be attributed to NO_2 emissions being too low at the observed plume location.~~

4.3.3 Summary

Large ozone biases are seen for both M270 and M296, where the model data show large overpredictions when compared against the aircraft data at corresponding locations. The bias appears to be relatively consistent across the latitude and longitude ranges of the flights and does not show any particular correlation with location, although appears to decrease with altitude in flight M270. Potential under-prediction of model boundary layer height ~~identified~~ in flight M270 may be responsible for this altitude dependent ozone model bias, as well as the poor predication of NO_2 at elevated altitudes in~~and elucidates~~ the model.~~altitude dependence on the M270 ozone model bias.~~ It is of note that the model biases seen are expected to have been larger if the AQUM data was produced using emissions modified for the COVID-19 pandemic (Grange et al., 2021). During M296, enhanced concentration of NO_2 are seen downwind of important sources. Observations aloft are in reasonable agreement with the available ground-based observations, suggesting the airmass aloft is coupled with ground. Meteorological conditions are broadly consistent between the model and observations, which implies low emission~~emissions~~ estimates may be responsible for this negative ~~NO_2~~ model bias in this case. Variability~~Model variation~~ in modelled ozone appears~~is shown~~ to be dependent~~fluctuate based~~ on the number grid boxes encompassed by the flight track. It is expected that ozone concentration in higher resolution models (>~~(->~~12km) will better match variation in the airborne observational data, as model resolution moves towards natural scale variability.

~~It may be possible to use the aircraft observations to help identify sources of model bias, or to determine an ozone bias correction factor that can be applied to the model data.~~

5 Conclusions and future plans

A long-term, quality assured, dataset on the three-dimensional distribution of NO_2, O_3, SO_2, and fine mode $PM_{2.5}$ aerosol, including optical absorption and scattering properties, has been collected over the UK using the instrumented Met Office Atmospheric Survey Aircraft from ~~July~~ 2019 to April 2022. Observations allow for the evaluation of regional air quality models such as AQUM. A description of the MOASA measurement platform and instrumentation is presented, along with details of flight plans, designed to allow repeatable, comparable observation of pollutants.

63 flight sorties, totalling over 150 hours of sampling, were flown during the campaign. These flights include observations of city scale pollution over Birmingham and Manchester during two periods of intensive observations in June-July 2021 and January-February 2022, as well as long-term (2019 to 2022) observations over London, including central London overpasses (from October 2020).

Analysis of relative humidity, total particle counts~~, NO_2~~ and ~~NO_2~~SO_2 over the campaign shows that instrument precision did not limit the ability to sample the natural pollutant variability, at length scales down to 0.42 km. In contrast, both SO_2 data and variability is shown to be~~with the exception of SO_2, where~~ limited by instrument precision at ~~sensitivity dominated in~~ all length scales. Comparison of airborne to ground-based observations generally show good agreement between the observation platforms when the boundary layer is well mixed, regardless of observation technique. This is particularly true for observations of $PM_{2.5}$ which showed strong agreement with an r^2 of 0.9. Comparison of odd oxygen implies that ozone titration is the dominant chemical process throughout the atmosphere and helps explicate the complex vertical structures of O_3 and NO_2 observed throughout the column. These analyses demonstrate that there are no fundamental issues in employing these high-horizontally spatial resolution airborne observations over~~but~~ a wide range of potential applications, from examining model representation of complex chemical processes in the horizontal and vertical, to improving the accuracy of air quality exposure estimates and satellite product validation.~~few cases where enhanced SO_2 concentrations were encountered.~~

Preliminary comparison of aircraft, ground and mast-based observations with~~and~~ AQUM data also highlights~~show~~ the use~~utility~~ of the ~~MOASA Clean Air~~ database for air quality model evaluation work, to substantially augment sparse ground observations.~~.~~ For the two flights analysed (M270 and M296), we show several cases of model-observation discrepancy that provide handles for further investigation associated with biases in modelled O_3 and NO_2 concentrations, ~~and~~ boundary layer height ~~and representation of emissions in coarse resolution models.~~. We anticipate that ~~in addition to evaluation work,~~ the airborne dataset may also be useful for derivation of bias-correction factors that can be applied to model data during post processing.

This paper serves as a reference for all future database users. The MOASA Clean Air database is comprised of quality assured observations, presented in NetCDF format with~~and is accompanied by~~ robust metadata to ensure traceability and transparency of data.

~~**A Clean Air** **Data** is openly **Framework is currently under development which will host the data. Whilst the framework is under development, data is** **available** **by request.**~~

~~Appendices from CEDA "Collection of airborne atmospheric measurements for the MOASA Clean Air project" repository (DOI: 10.5285/0aa1ec0cf18e4065bdae8ae39260fe7d)~~

Appendices

Appendix A: AQ Box schematic

The Air Quality box, as introduced in section 2.1 and shown schematically in figure A1, houses the POPS and TAP instruments, as well as actuated valves and flow controllers which control the sample flow to instruments.

Appendix B: ~~POPS calibration~~

~~Appendix C:~~ Index of refraction

$\omega 0_{nt}$ is determined by calculating the average single scattering albedo over the same flight transect as $\omega 0_{psd}$. First, the Virkkula-corrected TAP (absorption) data is smoothed to a 10 second triangular window to match the Muller-corrected nephelometer (scattering) data. The scattering and absorption ÅngstrÖm exponents (SAE and AAE, respectively), calculated as per equation C1, were used to adjust the multi-wavelength nephelometer (λ = 635, 525 and 450 nm) and TAP (λ = 652, 528 and 467 nm) instruments to the POPS wavelength (λ = 405 nm) using equation C2 (Perim De Faria et al., 2021). Uncertainties in derivation of AAE (from potential asynchronous sampling response times and flow rates) were reduced by applying maximum and minimum bounds estimated by considering the extremes of expected ambient AE values. Here, the AAE upper and lower bounds are 3 and 0.7, respectively, AAE is removed when raw red absorption < 1 Mm^{-1} and the AAE is set to 1.5 if the difference between absorption channels is < 1 Mm^{-1}. For the SAE, upper and lower bounds are 2.5 and 0.5, respectively, SAE is removed when raw red absorption < 10 Mm^{-1} and the AAE is set to 0.5 if the difference between scattering channels is < 1 Mm^{-1}. The data is then further averaged over 30 seconds to minimise variability from instrument noise/precision and any mismatch of data. To minimise uncertainties in wavelength correction using the ÅngstrÖm exponents, $\omega 0_{nt}$ is derived from the blue wavelengths only, using equation C3.

$$AE = \frac{-\log\left(\frac{AOCt_{\lambda 1}}{AOC_{\lambda 2}}\right)}{\log\left(\frac{\lambda 1}{\lambda 2}\right)}$$

Equation C1: where AE is the ÅngstrÖm exponent, AOC = Aerosol Optical coefficient (scattering or absorption) and λ_1 and λ_2 are wavelengths pairs.

$$AOC_{\lambda_{405}} = AOC_{\lambda i}\left(\frac{\lambda_{405}}{\lambda_i}\right)^{-AE}$$

Equation C2: where λ_{405} is the POPS wavelength (nm), λ_i is the wavelength of the given scattering or absorption coefficient and AE is the ÅngstrÖm exponent.

$$\omega 0_{nt} = \frac{\overline{scat\_blue}_{\lambda_{405}}}{\overline{scat\_blue}_{\lambda_{405}} + \overline{abs\_blue}_{\lambda_{405}}}$$

Equation C3: where the bar indicates the 30 second rolling average, for scattering (scat) and absorption (abs) for the blue wavelength nephelometer and TAP channels, converted to POPS wavelength (λ_{405}).

Determining ω0 using separate instruments with different uncertainties and principles can lead to potentially significant errors and biases (Perim De Faria et al., 2021). The uncertainty in the $\omega 0_{nt}$ calculations is related to the corresponding uncertainties in the scattering and absorption coefficients (Peers et al., 2019) measured by the nephelometer (4% at 450 nm, 2% at 525 nm and 5% at 635 nm, Müller et al., 2011) and TAP (30%, Ogren et al., 2017). These total measurement uncertainties are propagated according to appendix A of Perim De Faria et al., 2021 to give an uncertainty for $\omega 0_{nt}$ (equation C4).

$$\Delta\omega = \sqrt{\left(\frac{\sigma_{sc}}{(\sigma_{sc} + \sigma_{a})^2} \cdot \Delta\sigma_{sc}\right)^2 + \left(\frac{\sigma_{a}}{(\sigma_{sc} + \sigma_{a})^2} \cdot \Delta\sigma_{a}\right)^2}$$

Equation C4: Error propagation for $\omega 0_{nt}$, where σ_{sc} is independent scattering and σ_a is independent absorption coefficients.

ω0 is not very sensitive to the real part of the index of refraction, and as such the real part of the estimated index of refraction is not very well constrained (Peers et al., 2019). Figure B1~~C1~~ shows $\omega 0_{psd}$ derived using IOR=1.615+0.012j and IOR=1.59+0.012j which both yield a mean $\omega 0_{psd}$ of 0.917. As such, we use a real aspect of 1.59 as derived by McMeeking et al., 2012 during their airborne measurement campaign over London, UK in 2009. Where insufficient data is available to enable calculation of the ω0 and thus IOR, an IOR of 1.59+0.0j is adopted. The uncertainties associated with applying a flight-mean IOR is investigated in more depth in the following case study.

Section 2.7 describes the processing applied to particle sizing measurements to account for sizing errors caused by differences in the IOR between the calibrant and ambient particles. The method applies corrections based on the assumption of a single ambient IOR per flight, which was derived via an iterative process based on achieving closure with independent observations of particles single scattering albedo. In this section we undertake a sensitivity study to evaluate the magnitude of error arising from the assumption of a flight-mean IOR, based on variability observed during an example flight: M270, a high-Density Plume Mapping sortie north of Cambridge, where a sequence of straight and level runs at altitudes from 0.30 to 1.32 km were performed (Fig B2~~C2~~ and table B1~~C1~~). The wide range of altitudes over a single flight allows examination of the impact of a potentially changing airmass with altitude on derivation of a flight mean IOR. Refer to Sect 4.3 for a description of meteorological conditions for this flight.

The range of measured single scattering albedos, $\omega 0_{nt}$ during flight M270 varied throughout the boundary layer (0.886 to 0.944, Fig B1~~C1~~ red crosses) and yielded a flight mean $\omega 0_{nt}$=0.921 ± 0.019σ (Fig B1~~C1~~, red line). These values fall within the range of single scattering albedo's observed by McMeeking et al., 2011 during airborne observations over London (typically from 0.85 in urban plumes to 0.95 in regional pollution and background aerosol).

A flight mean $\omega 0_{psd}$=0.917±0.10 σ (Fig B1~~C1~~, blue line) was calculated using a particle size distribution (PSD) corrected with an optimally derived IOR=1.59+0.12j (herein referred to as IOR_{DER}). To examine sensitivity in

particle sizing due to variability in observed ω0 throughout the column, we also undertook PSD corrections based on achieving closure between $\omega 0_{psd}$ and the maximum observed $\omega 0_{nt}$ (IOR_{MAX}, 1.59+0.008j), minimum $\omega 0_{nt}$ (IOR_{MIN}, 1.59+0.016j) and an uncorrected PSD (retains the calibrant (PSL) IOR; IOR_{PSL}, 1.615+0.001j), shown as the grey dotted, dashed and dash-dot lines, respectively, on Fig B1~~C1~~.

Regression analysis (Fig B3~~C3~~, left column) of normalised PSD's corrected to IOR_{MIN} (top) IOR_{MAX} (middle) and IOR_{PSL} (bottom) against IOR_{DER} show good agreement, with r^2 of 0.9998, 0.9980 and 0.9983, respectively. Mean differences between IOR_{MIN}:IOR_{DER} , IOR_{MAX}:IOR_{DER} and IOR_{PSL}:IOR_{DER} (Fig B3~~C3~~, right column) are 9%, 10% and 23%, respectively. The comparatively large uncertainty between corrected and uncorrected size distributions underlines the importance of accounting for IOR corrections when making ambient aerosol measurements. Mean differences in all comparisons are largest where Dp ≈> 0.4 µm (PSD bin 15). Particle sizes in this region are comparable to the wavelength of light of the POPS (405 nm), which are the most efficient at scattering shortwave radiation and sizes larger than this can be influenced by Mie resonances (Liu and Daum, 2000).

Flight M270 was chosen based on it showing significant variability compared to other Clean Air flights; uncertainty in using a flight-mean IOR for less varying flights is expected to be less. For example, flight M302, a typical London survey on 22nd July 2021, performed numerous runs at altitudes≈0.5km and yields a difference of <2% between distributions corrected by IOR_{MIN} and IOR_{MAX}.

In summary, we conclude that use of a flight-mean IOR approach in correcting size distribution data introduces modest uncertainty of <10% compared to applying a variable IOR approach.

Appendix C~~D~~: PM2.5 composition and density

As discussed in section 2.8, mass concentration ($PM_{2.5}$) is derived from particle volume using the mean of a range of UK field experiments, which are detailed in table C1.

Appendix D~~E~~: M296 runs 2 and 3

Figure D1 shows model and observed NO_2 concentration throughout the second and third stacked box patterns performed around Birmingham during M296. Here, we see the intermediate stages of the plume as it begins to transition from the western quadrant of the city to the southeast with increasing altitude and time. As with runs 1 and 4, comparison of NO_2 aloft with average surface-level observations show similar concentrations and the plume is not captured by the model.

~~**Data availability**~~

~~Data is openly available from CEDA "Collection of airborne atmospheric measurements for the MOASA Clean Air project" repository (DOI: 10.5285/0aa1ec0cf18e4065bdae8ae39260fe7d)~~

~~Author~~Appendix F: NetCDF variables~~Author~~ **contribution**

JK, AW, DT and JB instrumented the MOASA. JK, AW, KW, JL, NN, ES and AM developed and planned flight sorties, and JK, AW and KW carried them out. AM designed, developed, and applied the post-flight quality assurance and processing software, with nephelometer, TAP and NO_2 (including development of the pressure dependent baseline correction) modules adapted from original code by Kate Szpek, Nick Davies/JL, and JL respectively. ES provided the AQUM model data and ES and BD assisted the observation/model comparison. AM, JL and SA conceptualised the analysis (Sect 4) and AM performed the formal analysis. MH devised and wrote the SPF Clean Air research programme of which the MOASA flights are an integral part, acquired the financial support for the project and also contributed to the original concept of a prolonged observation campaign. NN lead the conceptualization of MOASA involvement in the IOP's. AM prepared the manuscript with contributions from JL, ES, JK, KW, SA and MH.

The authors declare that they have no conflict of interest.

~~7~~ Acknowledgments

The MOASA Clean Air project is supported by the Clean Air programme which is jointly delivered by the Natural Environment Research Council (NERC) and the Met Office, with the Economic and Social Research Council (ESRC), Engineering and Physical Sciences Research Council (EPSRC), Innovate UK, Medical Research Council (MRC), National Physical Laboratory (NPL), Science and Technology Facilities Research Council (STFC), Department for Environment, Food and Rural Affairs (Defra), Department for Health and Social Care (DHSC), Department for Transport (DfT), Scottish Government and Welsh Government.

The authors acknowledge and thank Alto Aerospace for efforts in delivering flight operations, the Met Office Guidance Unit who have supported flight planning throughout, Kate Szpek and Nick Davies, who's nephelometer and TAP (respectively) processing software were adapted for this work, and Debbie O'Sullivan for creating Fig 1.

References

Aerodyne Research Inc.: CAPS NO2 Monitor, , (CSST_INST_1_1), 1–2 [online] Available from: www.aerodyne.com, n.d.

Air Quality Expert Group: Fine Particulate Matter (PM 2 . 5) in the United Kingdom. [online] Available from: https://uk-air.defra.gov.uk/assets/documents/reports/cat11/1212141150_AQEG_Fine_Particulate_Matter_in_the_UK.pdf, 2012.

Air Quality Expert Group: Estimation of changes in air pollution emissions, concentrations and exposure during the COVID-19 outbreak in the UK, UK Air Inf. Resour., (June), 1–57, 2020.

Beecken, J., Mellqvist, J., Salo, K., Ekholm, J. and Jalkanen, J. P.: Airborne emission measurements of SO2,

NOx and particles from individual ships using a sniffer technique, Atmos. Meas. Tech., 7(7), 1957–1968, doi:10.5194/amt-7-1957-2014, 2014.

Bond, T. C. and Bergstrom, R. W.: Light absorption by carbonaceous particles: An investigative review, Aerosol Sci. Technol., 40(1), 27–67, doi:10.1080/02786820500421521, 2006.

Bond, T. C., Anderson, T. L. and Campbell, D.: Calibration and Intercomparison of Filter-Based Measurements of Visible Light Absorption by Aerosols, Aerosol Sci. Technol., 30(6), 582–600, doi:10.1080/027868299304435, 1999.

Brechtel Manufacturing Inc: Model 1200 Isokinetic Aerosol Inlet System Manual ver. 8.0, 2011.

Crilley, L. R., Singh, A., Kramer, L. J., Shaw, M. D., Alam, M. S., Apte, J. S., Bloss, W. J., Hildebrandt Ruiz, L., Fu, P., Fu, W., Gani, S., Gatari, M., Ilyinskaya, E., Lewis, A. C., Ng'ang'a, D., Sun, Y., Whitty, R. C. W., Yue, S., Young, S. and Pope, F. D.: Effect of aerosol composition on the performance of low-cost optical particle counter correction factors, Atmos. Meas. Tech., 13(3), 1181–1193, doi:10.5194/amt-13-1181-2020, 2020.

Dassios, K. G. and Pandis, S. N.: The mass accommodation coefficient of ammonium nitrate aerosol, Atmos. Environ., 33(18), 2993–3003, doi:10.1016/S1352-2310(99)00079-5, 1999.

Davies, N. W., Fox, C., Szpek, K., Cotterell, M. I., Taylor, J. W., Allan, J. D., Williams, P. I., Trembath, J., Haywood, J. M. and Langridge, J. M.: Evaluating biases in filter-based aerosol absorption measurements using photoacoustic spectroscopy, Atmos. Meas. Tech., 12(6), 3417–3434, doi:10.5194/amt-12-3417-2019, 2019.

DEFRA: Clean air strategy 2019. [online] Available from: https://www.gov.uk/government/publications/clean-air-strategy-2019, 2019.

Dewline[internet]: DewLine^{TM}, [online] Available from: https://twobtech.com/dewline.html (Accessed 15 May 2020), n.d.

Ecotech: Aurora3000 Integrating Nephelometer with backscatter, user manual v1.3, [online] Available from: https://www.ecotech.com/product/particulates/aerosol-research-instruments/aurora-3000/, 2009.

El-Harbawi, M.: Air quality modelling, simulation, and computational methods: a review, Environ. Rev., 21, doi:https://doi.org/10.1139/er-2012-0056, 2013.

Frie, A. L. and Bahreini, R.: Refractive index confidence explorer (RICE): A tool for propagating uncertainties through complex refractive index retrievals from aerosol particles, Aerosol Sci. Technol., 55(6), 703–717, doi:10.1080/02786826.2021.1895428, 2021.

Gao, R. S., Telg, H., McLaughlin, R. J., Ciciora, S. J., Watts, L. A., Richardson, M. S., Schwarz, J. P., Perring, A. E., Thornberry, T. D., Rollins, A. W., Markovic, M. Z., Bates, T. S., Johnson, J. E. and Fahey, D. W.: A light-weight, high-sensitivity particle spectrometer for PM2.5 aerosol measurements, Aerosol Sci. Technol., 50(1), 88–99, doi:10.1080/02786826.2015.1131809, 2016.

Grange, S. K., Lee, J. D., Drysdale, W. S., Lewis, A. C., Hueglin, C., Emmenegger, L. and Carslaw, D. C.: COVID-19 lockdowns highlight a risk of increasing ozone pollution in European urban areas, Atmos. Chem. Phys., 21(5), 4169–4185, doi:10.5194/acp-21-4169-2021, 2021.

Hagan, D. and Kroll, J.: Assessing the accuracy of low-cost optical particle sensors using a physics-based approach, Atmos. Meas. Tech. Discuss., 1–36, doi:10.5194/amt-2020-188, 2020.

Harrison, R. M., Jones, A. M. and Lawrence, R. G.: Major component composition of PM10 and PM2.5 from roadside and urban background sites, Atmos. Environ., 38(27), 4531–4538, doi:10.1016/j.atmosenv.2004.05.022, 2004.

Haywood, J.: Prediction of visibility and aerosol within the operationalMet Office Unified Model.II: Validation of model performance using observational data, Q. J. R. Meteorol. Soc., (134), 1817–1832, doi:10.1002/qj.275,

2008.

Hoon Jung, C., Jung Shin, H., Yi Lee, J., Pyo Kim, Y., Pitari, G. and Curci, G.: Sensitivity and Contribution of Organic Aerosols to Aerosol Optical Properties Based on Their Refractive Index and Hygroscopicity, , doi:10.3390/atmos7050065, 2016.

Kebabian, P. L., Herndon, S. C. and Freedman, A.: Detection of nitrogen dioxide by cavity attenuated phase shift spectroscopy, Anal. Chem., 77(2), 724–728, doi:10.1021/ac048715y, 2005.

Lafon, S., Sokolik, I. N., Rajot, J. L., Caquincau, S. and Gaudichet, A.: Characterization of iron oxides in mineral dust aerosols: Implications for light absorption, J. Geophys. Res. Atmos., 111(21), 1–19, doi:10.1029/2005JD007016, 2006.

Langridge, J. M., Ball, S. M., Shillings, A. J. L. and Jones, R. L.: A broadband absorption spectrometer using light emitting diodes for ultrasensitive, in situ trace gas detection, Rev. Sci. Instrum., 79(12), doi:10.1063/1.3046282, 2008.

Langridge, J. M., Lack, D., Brock, C. A., Bahreini, R., Middlebrook, A. M., Neuman, J. A., Nowak, J. B., Perring, A. E., Schwarz, J. P., Spackman, J. R., Holloway, J. S., Pollack, I. B., Ryerson, T. B., Roberts, J. M., Warneke, C., De Gouw, J. A., Trainer, M. K. and Murphy, D. M.: Evolution of aerosol properties impacting visibility and direct climate forcing in an ammonia-rich urban environment, J. Geophys. Res. Atmos., 117(6), 1–17, doi:10.1029/2011JD017116, 2012.

Liu, X., Chance, K., Sioris, C. E., Spurr, R. J. D., Kurosu, T. P., Martin, R. V. and Newchurch, M. J.: Ozone profile and tropospheric ozone retrievals from the Global Ozone Monitoring Experiment: Algorithm description and validation, J. Geophys. Res. Atmos., 110(20), 1–19, doi:10.1029/2005JD006240, 2005.

Liu, Y. and Daum, P. H.: The effect of refractive index on size distributions and light scattering coefficients derived from optical particle counters, J. Aerosol Sci., 31(8), 945–957, doi:10.1016/S0021-8502(99)00573-X, 2000.

Manisalidis, I., Stavropoulou, E., Stavropoulos, A. and Bezirtzoglou, E.: Environmental and Health Impacts of Air Pollution: A Review, Front. Public Heal., 8(February), 1–13, doi:10.3389/fpubh.2020.00014, 2020.

McMeeking, G. R., Morgan, W. T., Flynn, M., Highwood, E. J., Turnbull, K., Haywood, J. and Coe, H.: Black carbon aerosol mixing state, organic aerosols and aerosol optical properties over the United Kingdom, Atmos. Chem. Phys., 11(17), 9037–9052, doi:10.5194/acp-11-9037-2011, 2011.

McMeeking, G. R., Bart, M., Chazette, P., Haywood, J. M., Hopkins, J. R., McQuaid, J. B., Morgan, W. T., Raut, J. C., Ryder, C. L., Savage, N., Turnbull, K. and Coe, H.: Airborne measurements of trace gases and aerosols over the London metropolitan region, Atmos. Chem. Phys., 12(11), 5163–5187, doi:10.5194/acp-12-5163-2012, 2012.

Molina, M. J. and Molina, L. T.: Megacities and atmospheric pollution, J. Air Waste Manag. Assoc., 54(6), 644–680, doi:10.1080/10473289.2004.10470936, 2004.

Müller, T., Laborde, M., Kassell, G. and Wiedensohler, A.: Design and performance of a three-wavelength LED-based total scatter and backscatter integrating nephelometer, Atmos. Meas. Tech., 4(6), 1291–1303, doi:10.5194/amt-4-1291-2011, 2011.

Müller, T., Virkkula, A. and Ogren, J. A.: Constrained two-stream algorithm for calculating aerosol light absorption coefficient from the Particle Soot Absorption Photometer, Atmos. Meas. Tech., 7(12), 4049–4070, doi:10.5194/amt-7-4049-2014, 2014.

Neal, L. S., Agnew, P., Moseley, S., Ordóñez, C., Savage, N. H. and Tilbee, M.: Application of a statistical post-processing technique to a gridded, operational, air quality forecast, Atmos. Environ., 98, 385–393, doi:10.1016/j.atmosenv.2014.09.004, 2014.

NOAA: CAMEO Chemicals[Internet], CAMEO Chem. version 2.7.1 rev 3. [online] Available from: https://cameochemicals.noaa.gov/chemical/25006 (Accessed 23 November 2021), n.d.

Nowak, J. B., Neuman, J. A., Bahreini, R., Brock, C. A., Middlebrook, A. M., Wollny, A. G., Holloway, J. S., Peischl, J., Ryerson, T. B. and Fehsenfeld, F. C.: Airborne observations of ammonia and ammonium nitrate formation over Houston, Texas, J. Geophys. Res. Atmos., 115(22), 1–12, doi:10.1029/2010JD014195, 2010.

Ogren, J. A., Wendell, J., Andrews, E. and Sheridan, P. J.: Continuous light absorption photometer for long-Term studies, Atmos. Meas. Tech., 10(12), 4805–4818, doi:10.5194/amt-10-4805-2017, 2017.

OSCA: No Title, [internet] [online] Available from: www.ukcleanair.org (Accessed 1 December 2021), 2020.

Peers, F., Francis, P., Fox, C., Abel, S. J., Szpek, K., Cotterell, M. I., Davies, N. W., Langridge, J. M., Meyer, K. G., Platnick, S. E. and Haywood, J. M.: Observation of absorbing aerosols above clouds over the south-east Atlantic Ocean from the geostationary satellite SEVIRI-Part 1: Method description and sensitivity, Atmos. Chem. Phys., 19(14), 9595–9611, doi:10.5194/acp-19-9595-2019, 2019.

Perim De Faria, J., Bundke, U., Freedman, A., Onasch, T. B. and Petzold, A.: Laboratory validation of a compact single-scattering albedo (SSA) monitor, Atmos. Meas. Tech., 14(2), 1635–1653, doi:10.5194/amt-14-1635-2021, 2021.

Petzold, A., Thouret, V., Gerbig, C., Zahn, A., Brenninkmeijer, C. A. M., Gallagher, M., Hermann, M., Pontaud, M., Ziereis, H., Boulanger, D., Marshall, J., NéDélec, P., Smit, H. G. J., Friess, U., Flaud, J. M., Wahner, A., Cammas, J. P., Volz-Thomas, A., Thomas, K., Rohs, S., Bundke, U., Neis, P., Berkes, F., Houben, N., Berg, M., Tappertzhofen, M., Blomel, T., Pätz, W., Filges, A., Boschetti, F., Verma, S., Baum, S., Athier, G., Cousin, J. M., Sauvage, B., Blot, R., Clark, H., Gaudel, A., Gressent, A., Auby, A., Fontaine, A., Gautron, B., Bennouna, Y., Petetin, H., Karcher, F., Abonnel, C., Dandin, P., Beswick, K., Wang, K. Y., Rauthe-Schöch, A., Baker, A. K., Riede, H., Gromov, S., Zimmermann, P., Thorenz, U., Scharffe, D., Koeppel, C., Slemr, F., Schuck, T. J., Umezawa, T., Ditas, J., Cheng, Y., Schneider, J., Williams, J., Neumaier, M., Christner, E., Fischbeck, G., Safadi, L., Petrelli, A., Gehrlein, T., Heger, S., Dyroff, C., Weber, S., Assmann, D., Rubach, F., Weigelt, A., Stratmann, G., Stock, P., Penth, L., Walter, D., Heue, K. P., Allouche, Y., Marizy, C., Hermira, J., Bringtown, S., Saueressig, G., Seidel, N., Huf, M., Waibel, A., Franke, H., Klaus, C., Stosius, R., Baumgardner, D., Braathen, G., Paulin, M. and Garnett, N.: Global-scale atmosphere monitoring by in-service aircraft - current achievements and future prospects of the European Research Infrastructure IAGOS, Tellus, Ser. B Chem. Phys. Meteorol., 6(1), 1–24, doi:10.3402/tellusb.v67.28452, 2015.

PubChem: PubChem[Internet], [online] Available from: https://pubchem.ncbi.nlm.nih.gov/source/hsdb/902, n.d.

Rosenberg, P. D., Dean, A. R., Williams, P. I., Dorsey, J. R., Minikin, A., Pickering, M. A. and Petzold, A.: Particle sizing calibration with refractive index correction for light scattering optical particle counters and impacts upon PCASP and CDP data collected during the Fennec campaign, Atmos. Meas. Tech., 5(5), 1147–1163, doi:10.5194/amt-5-1147-2012, 2012.

Savage, N. H., Agnew, P., Davis, L. S., Ordóñez, C., Thorpe, R., Johnson, C. E., O'Connor, F. M. and Dalvi, M.: Air quality modelling using the Met Office Unified Model (AQUM OS24-26): Model description and initial evaluation, Geosci. Model Dev., 6(2), 353–372, doi:10.5194/gmd-6-353-2013, 2013.

Solazzo, E., Bianconi, R., Pirovano, G., Moran, M. D., Vautard, R., Hogrefe, C., Appel, K. W., Matthias, V., Grossi, P., Bessagnet, B., Brandt, J., Chemel, C., Christensen, J. H., Forkel, R., Francis, X. V., Hansen, A. B., McKeen, S., Nopmongcol, U., Prank, M., Sartelet, K. N., Segers, A., Silver, J. D., Yarwood, G., Werhahn, J., Zhang, J., Rao, S. T. and Galmarini, S.: Evaluating the capability of regional-scale air quality models to capture the vertical distribution of pollutants, Geosci. Model Dev., 6(3), 791–818, doi:10.5194/gmd-6-791-2013, 2013.

The National Meteorological Library: Daily weather summary | September 2020 Daily Weather Summaries for September 2020, , (September), 2020.

Thermo Scientific: Thermo Scientific Model 43 i Sulfur Dioxide Analyzer — pulsed fluorescence gas analyzer, [online] Available from: https://www.thermofisher.com/document-connect/document-connect.html?url=https://assets.thermofisher.com/TFS-Assets%2FLSG%2FSpecification-Sheets%2FEPM-43i-Datasheet.pdf, n.d.

UKRI: Integrated Research Observation System for Clean Air (OSCA), [internet] [online] Available from: https://gtr.ukri.org/projects?ref=NE%2FT001984%2F1 (Accessed 2 November 2021), 2021.

Veefkind, J. P., Aben, I., McMullan, K., Förster, H., de Vries, J., Otter, G., Claas, J., Eskes, H. J., de Haan, J. F., Kleipool, Q., van Weele, M., Hasekamp, O., Hoogeveen, R., Landgraf, J., Snel, R., Tol, P., Ingmann, P., Voors, R., Kruizinga, B., Vink, R., Visser, H. and Levelt, P. F.: TROPOMI on the ESA Sentinel-5 Precursor: A GMES mission for global observations of the atmospheric composition for climate, air quality and ozone layer applications, Remote Sens. Environ., 120(2012), 70–83, doi:10.1016/j.rse.2011.09.027, 2012.

Virkkula, A.: Calibration of the 3-wavelength particle soot absorption photometer (3λ PSAP) (Aerosol Science and Technology (2002) 39 (68-83)), Aerosol Sci. Technol., 44(8), 706–712, doi:10.1080/02786826.2010.482110, 2010.

Walters, D., Baran, A. J., Boutle, I., Brooks, M., Earnshaw, P., Edwards, J., Furtado, K., Hill, P., Lock, A., Manners, J., Morcrette, C., Mulcahy, J., Sanchez, C., Smith, C., Stratton, R., Tennant, W., Tomassini, L., Van Weverberg, K., Vosper, S., Willett, M., Browse, J., Bushell, A., Carslaw, K., Dalvi, M., Essery, R., Gedney, N., Hardiman, S., Johnson, B., Johnson, C., Jones, A., Jones, C., Mann, G., Milton, S., Rumbold, H., Sellar, A., Ujiie, M., Whitall, M., Williams, K. and Zerroukat, M.: The Met Office Unified Model Global Atmosphere 7.0/7.1 and JULES Global Land 7.0 configurations, Geosci. Model Dev., 12(5), 1909–1963, doi:10.5194/gmd-12-1909-2019, 2019.

Von Der Weiden, S. L., Drewnick, F. and Borrmann, S.: Particle Loss Calculator - A new software tool for the assessment of the performance of aerosol inlet systems, Atmos. Meas. Tech., 2(2), 479–494, doi:10.5194/amt-2-479-2009, 2009.

Wilson, K. L. and Birks, J. W.: Mechanism and elimination of a water vapor interference in the measurement of ozone by UV absorbance, Environ. Sci. Technol., 40(20), 6361–6367, doi:10.1021/es052590c, 2006.

World Health Organization: Evolution of WHO air quality guidelines., 2017.

Wyche, K. P., Nichols, M., Parfitt, H., Beckett, P., Gregg, D. J., Smallbone, K. L. and Monks, P. S.: Changes in ambient air quality and atmospheric composition and reactivity in the South East of the UK as a result of the COVID-19 lockdown, Sci. Total Environ., 755, doi:10.1016/j.scitotenv.2020.142526, 2021.

Yardley, R., Clark, T., Eaton, S., Gray, S., Hector, D., Loader, A., Madle, A., Stacey, B., Stratton, S. and Telfer, S.: Automatic Urban and Rural Network: Site Operator's Manual, , (1), 15 [online] Available from: https://shuspace.shu.ac.uk/bbcswebdav/pid-7749472-dt-content-rid-25936034_2/courses/77-600356-AF-20189/LSO_manual_2012_Part_A_Issue_1_final.pdf, 2012.

~~Main text~~ Figures

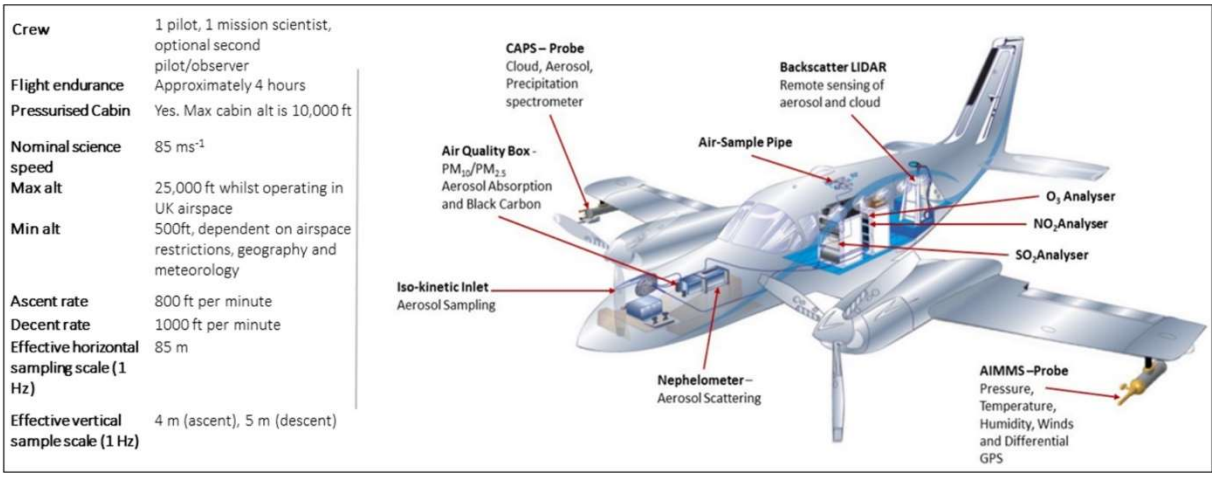

Figure 1: The Met Office Atmospheric Survey Aircraft with instrumentation. Image courtesy Debbie O'Sullivan, Met Office, 2021.

Figure 2: Clockwise starting top left: the AQ box (foreground) and nephelometer (background) in the MOASA nose bay; the aft instrumented rack housing the O_3, NO_2 and aerosol LIDAR control system; inside the AQ box; inside the cabin looking forward; the Brechtel isokinetic air sample inlet and nose bay of the MOASA.

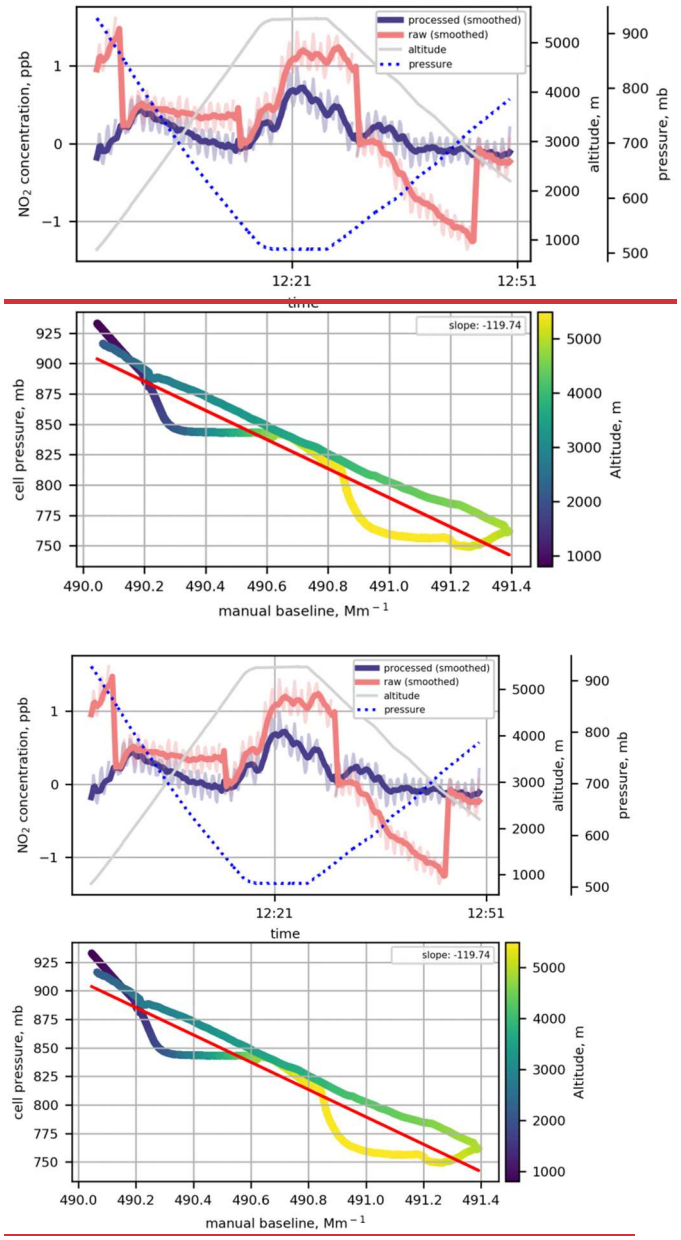

Figure 3: Top: timeseries of ~~raw (uncorrected)~~**unprocessed** and processed ~~(corrected)~~ NO_2 concentration. Oscillations seen in the raw and processed data during the filter test in are an artefact of the filter, which impacted performance of the instrument pump. These oscillations have been minimised by arbitrarily smoothing (60 second rolling) the data, for visualisation purposes only. Bottom: baseline against cell pressure, coloured by altitude, with a linear fit shown as~~**with**~~ a red~~**blue**~~ line. ~~All data from 11:55:00 to 12:50:00~~**Data obtained** during flight M304 ~~on 4th~~**in** November 2021~~,~~ ~~**and**~~ averaged over 10 second intervals.

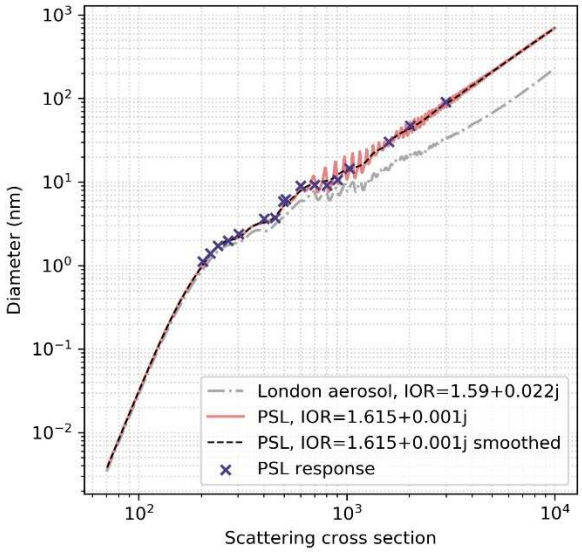

Figure 4: Theoretical MOASA POPS Mie responses for PSL calibrant (1.615+0.001j) and ambient aerosol over London: 1.59-0.022j (McMeeking et al., 2012). Crosses are PSL responses from calibration on 16th September 2021.

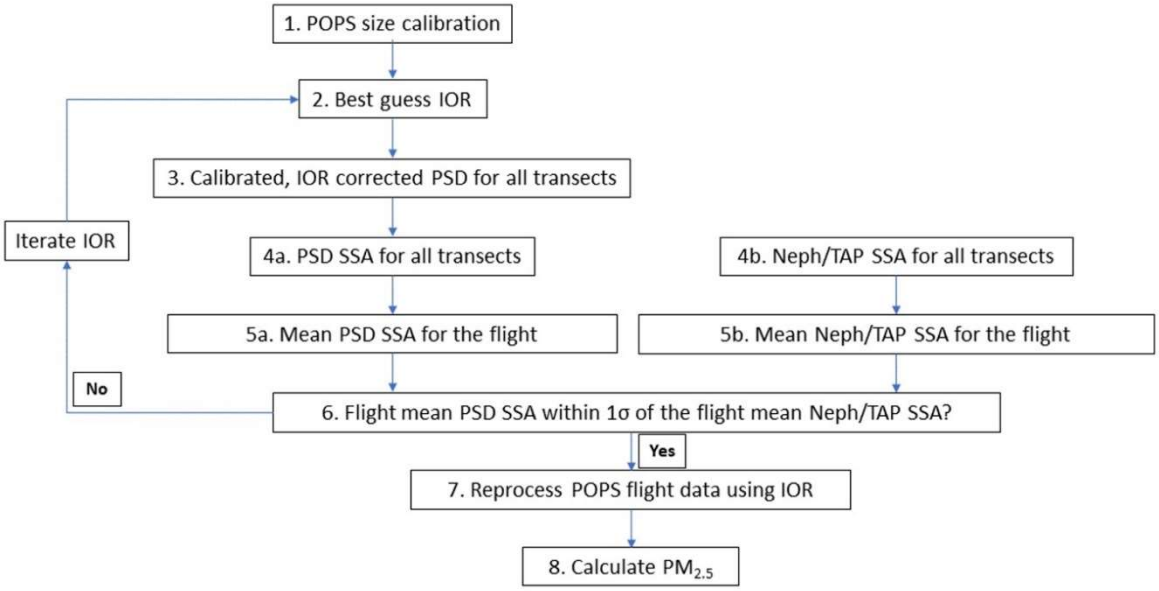

Figure 5: Process to estimate the IOR of the ambient sample by iteratively adjusting the index of refraction of the POPS size distribution measurements until the POPS single scattering albedo matches the single scattering albedo from the nephelometer and TAP.

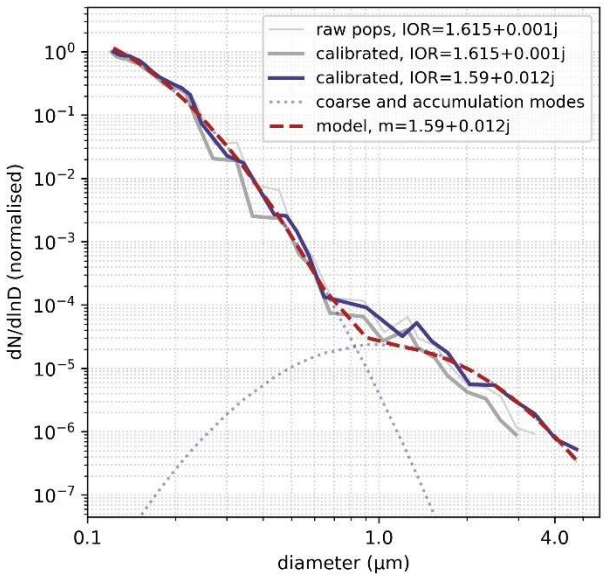

Figure 6: An example of raw, calibrated and calibrated with IOR-correction (IOR=1.59+0.12j) particle size distributions, where the Y axis is normalised to 1. Overlaid are lognormal accumulation and coarse modes (dotted) plus the combination of these lognormal modes (dashed) fitted to the calibrated with IOR correction (blue solid line) size distribution.

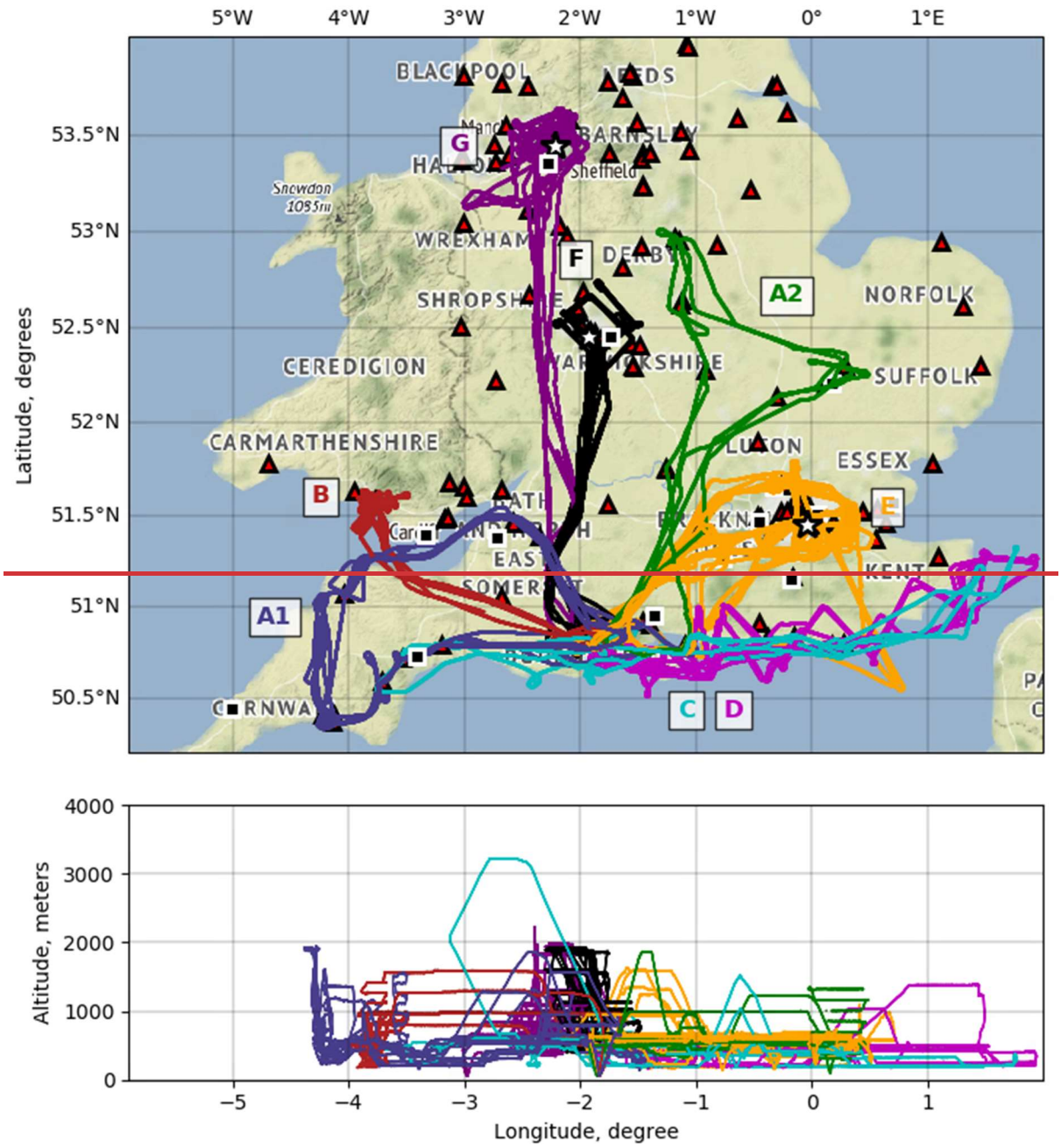

~~**Figure 7:** Horizontal (top) and vertical (bottom) spatial coverage of 63 MOASA Clean Air flights from 27/07/2019 (flight M247) to 11/04/2022 (flight M326). AURN sites are shown as triangles, airports as squares, stars are ground based supersites in Birmingham, Manchester and London. The annotations relate to the sortie type detailed in Fig.7 where A1 and A2 are Ground Network Surveys, B are High Density Plume Mapping flights, C are South Coast Surveys, D are Coastal Transition Surveys, E are London City Surveys and F and G are the Birmingham and Manchester, respectively, IOP flights. Map by Stamen Design, under CC BY 3.0. Data by OpenStreetMap, under ODbL.~~

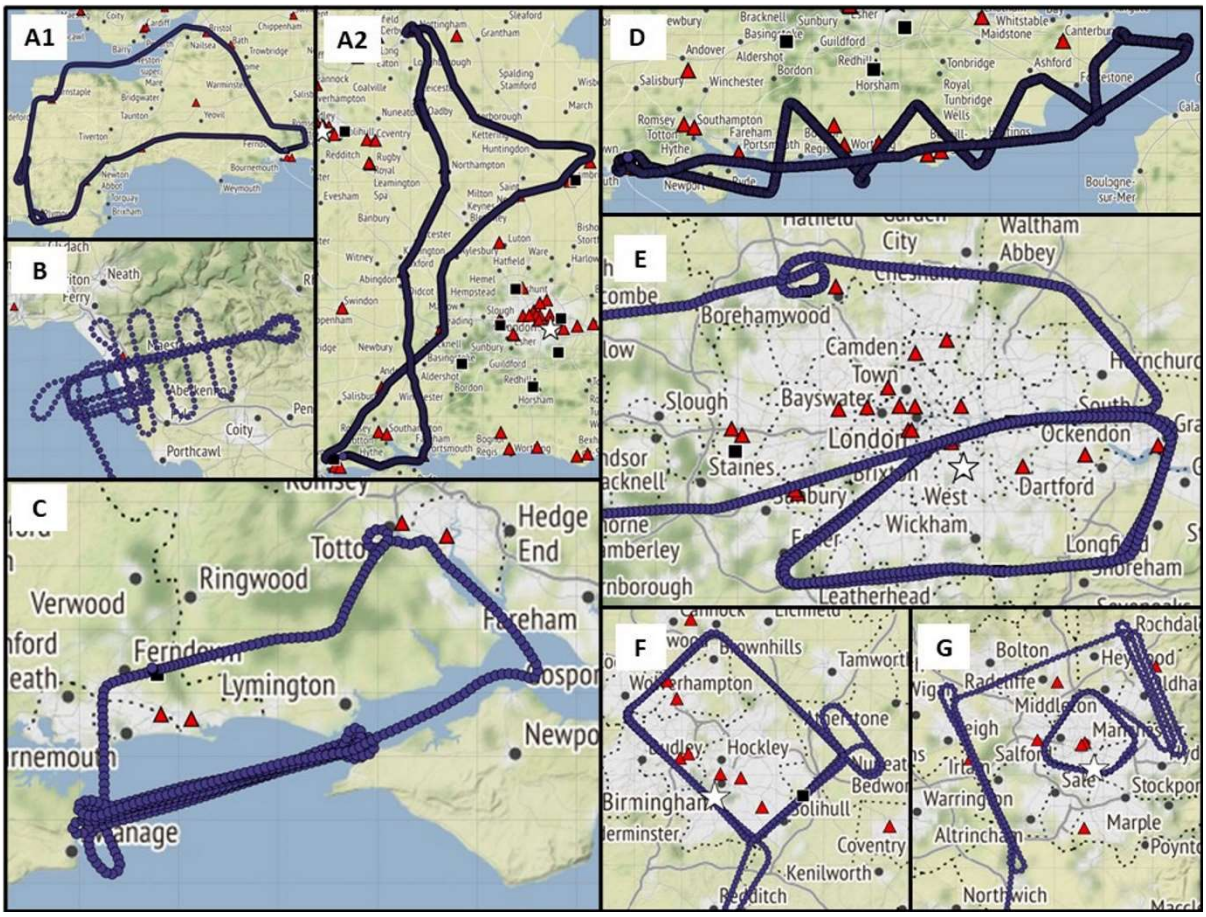

Figure 87: Aircraft flight tracks for a typical (A) ground network survey over the south west (A1) and east (A2), during M288 and M262 on 19th May 2021 and 10th January 2020, respectively, (B) high density vertical mapping over Port Talbot, South Wales, during M284 on 24th March 2021, (C) south coast survey flight, during M301 on 27th July 2021, with focus on overpasses of the Solent and Southampton water, (D) coastal transition flight, during M285 on 30th March 2021, (E) London city survey flight IOP, M297 on 2nd July 2021. (F) Birmingham IOP flight (left), during M296 on 1st July 2021, (G) a typical Manchester IOP flight, during M300 on 20th July 2021. AURN sites are shown as triangles, airports as squares, stars are ground based supersites in Birmingham, Manchester and London. The geographical location of each sortie is shown in figure 78. Map tiles by Stamen Design, under CC BY 3.0. Data by OpenStreetMap, under ODbL.

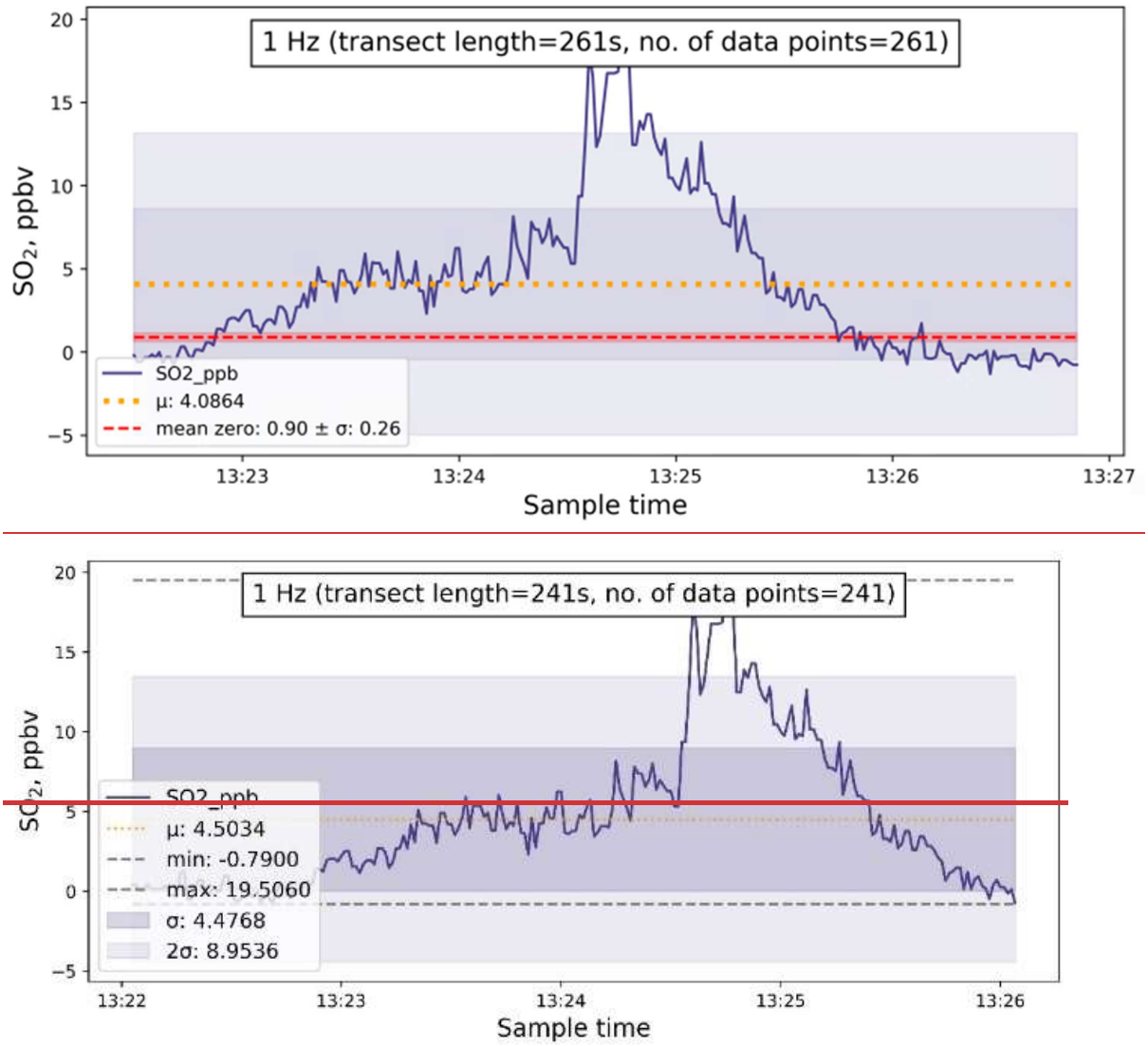

Figure 9: SO_2 timeseries from 13:22:30 – 13:26:50 during high density mapping flight M284. The solid blue line is SO_2 concentration in PPB, with the mean shown as the horizontal dotted line, with one and two standard deviations as the shaded grey areas. The mean SO_2 zero (0.9 ppb) is the dashed red line, with red shading showing one standard deviation of the mean.

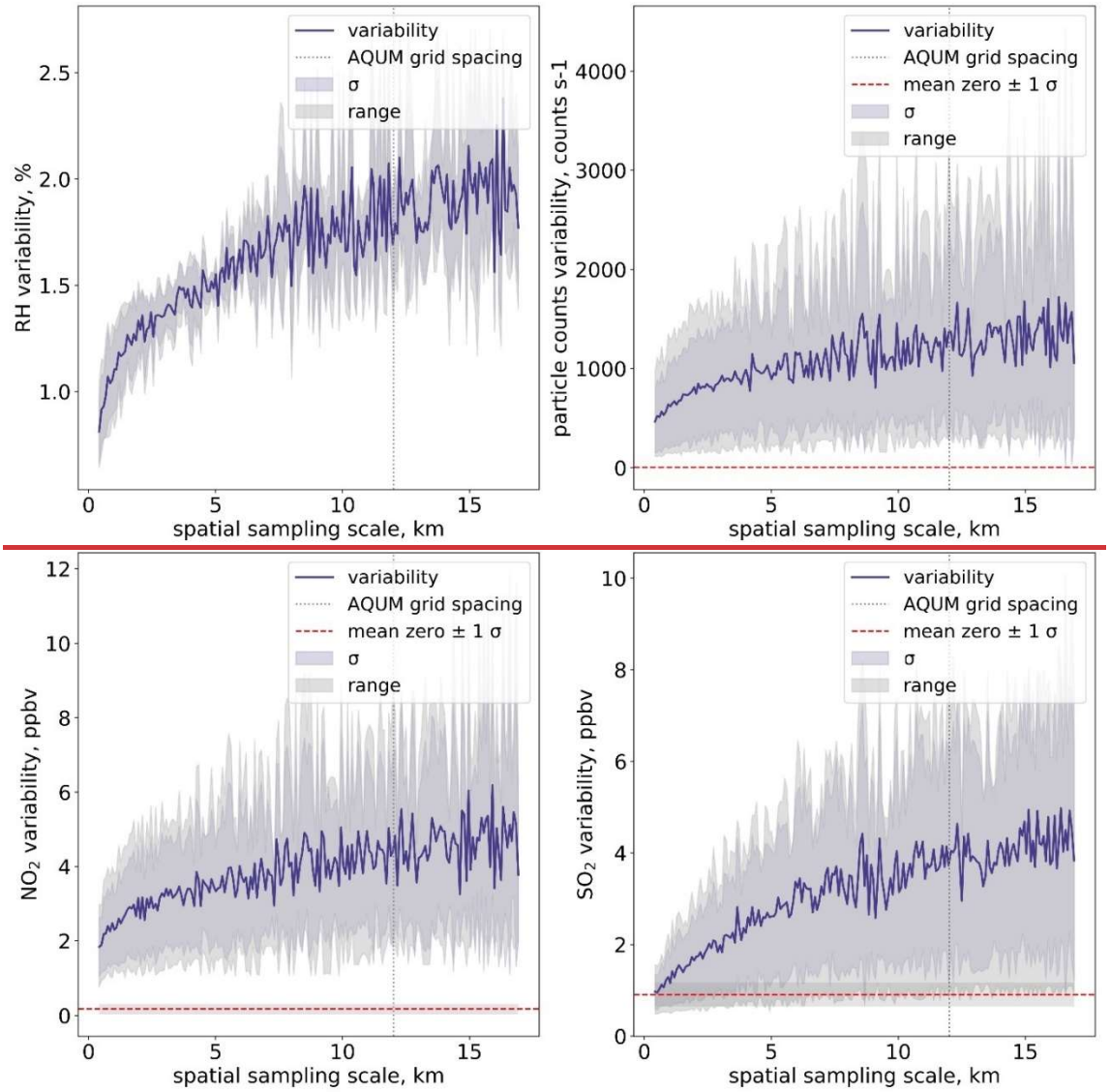
variability
AQUM grid spacing
σ
range
RH variability, %
spatial sampling scale, km
variability
AQUM grid spacing
mean zero ± 1 σ
σ
range
particle counts variability, counts s-1
spatial sampling scale, km
variability
AQUM grid spacing
mean zero ± 1 σ
σ
range
NO2 variability, ppbv
spatial sampling scale, km
variability
AQUM grid spacing
mean zero ± 1 σ
σ
range
SO2 variability, ppbv
spatial sampling scale, km

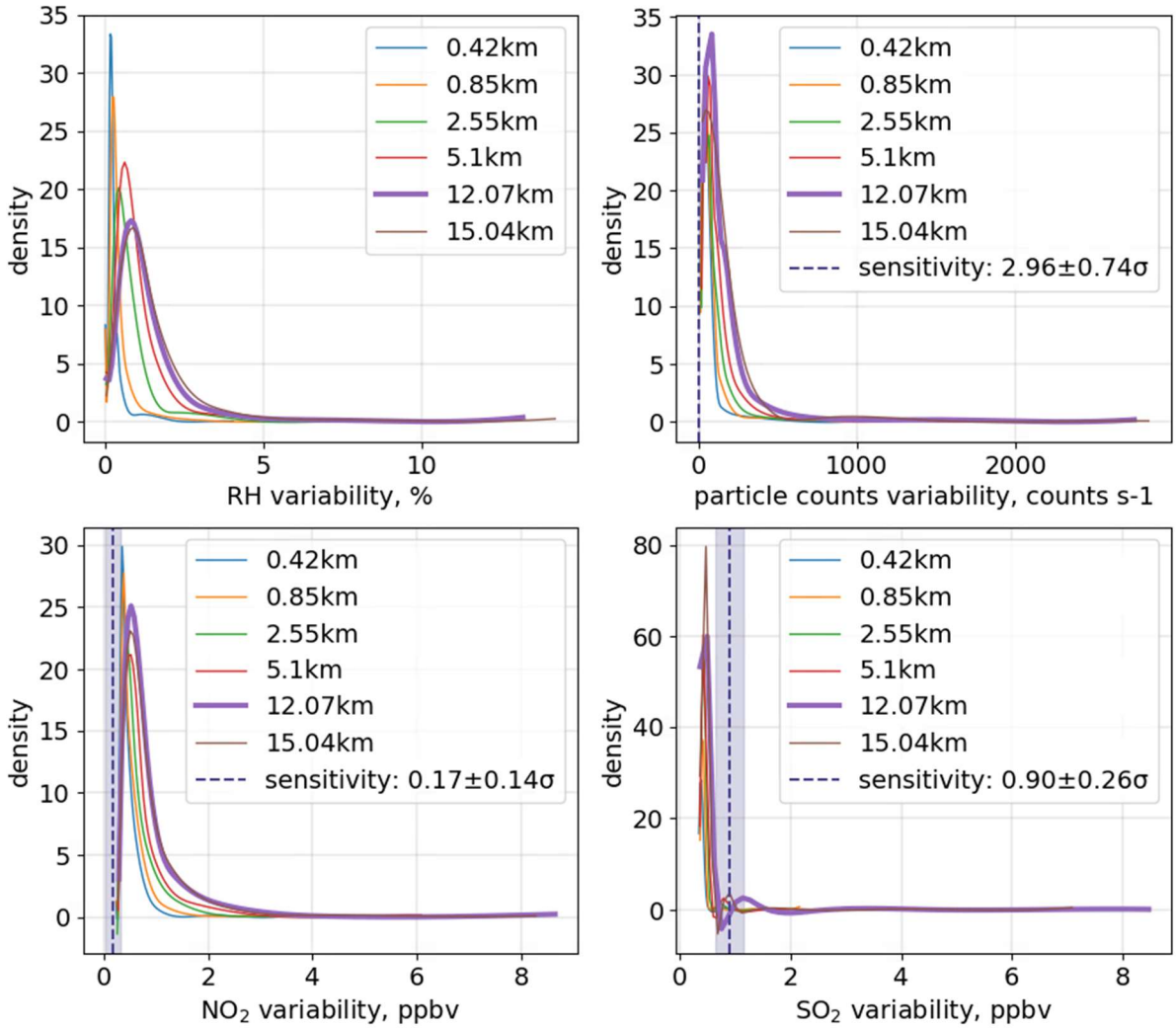

~~**Figure 10: Mean standard deviation (std, blue line) of relative humidity, particle counts, NO_2 and SO_2 over flight M284, as a function of spatial scale from 0.85 km to 17 km. The horizontal dashed red lines represent instrument precision (±1 σ) derived from ground-based zero tests (where available).**~~

Figure 10~~11~~: Density distributions of RH, particle counts, NO_2 and SO_2 variability ~~over the Clean Air campaign~~, for d_{int}= 0.42, 0.85, 2.55, 5.10, 12.07, and 15.04 km, for 322 straight and level runs over 63 flights of the MOASA Clean Air campaign. Vertical dashed lines show the instrument sensitivity ± 1 standard deviation.

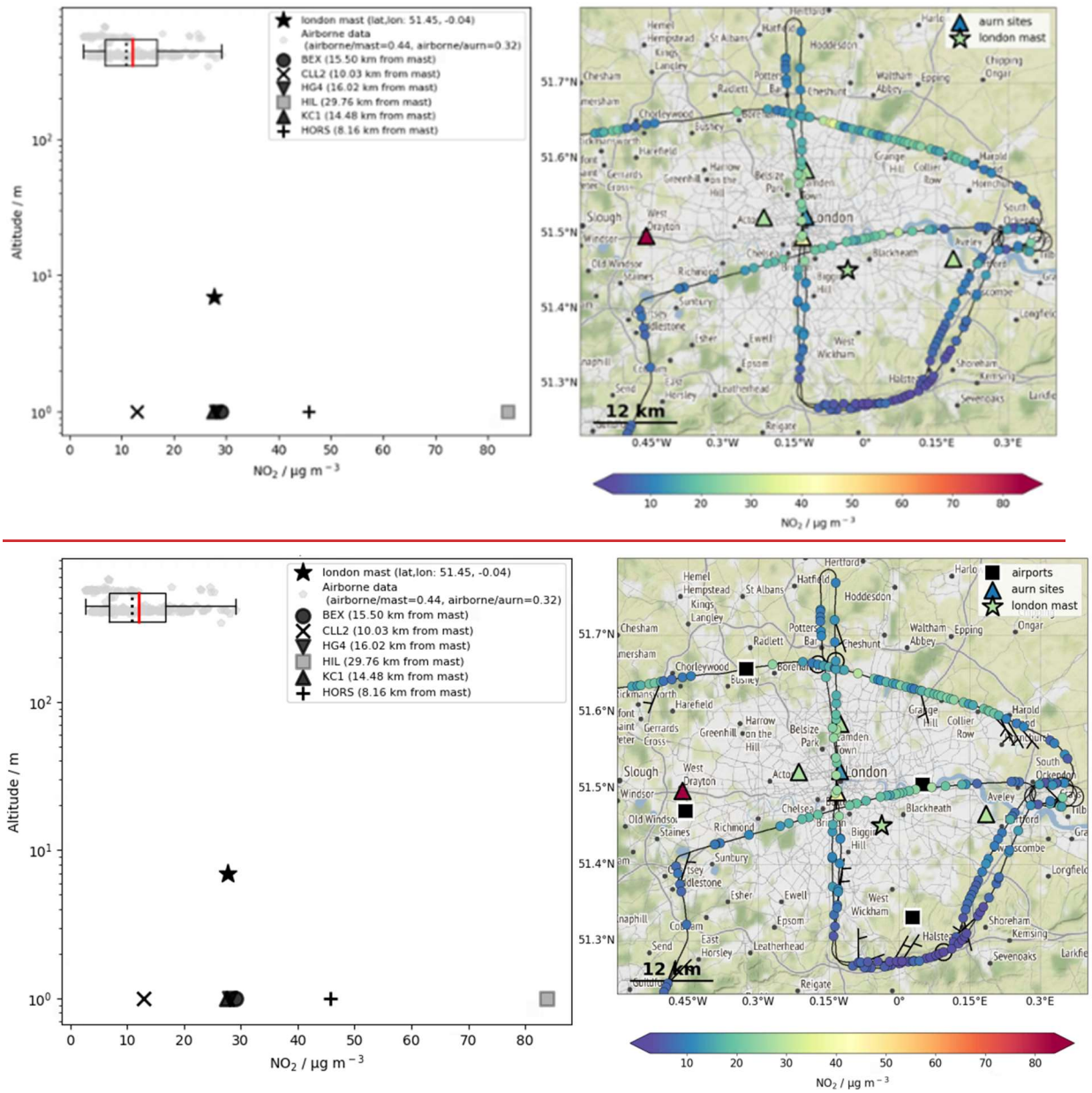

~~**Figure 12:** flight M325 on 24/03/2022. **Left**: Altitude profile, where airborne observations of NO_2 within Greater London are shown in grey and the boxplot represents the inter-quartile range, the data range (whiskers), the median (vertical dashed black line) and mean (vertical red solid line) of these data. The London IOP supersite is shown as a black star, and AURN ground sites within the region are shown as various markers (see key). Ratios of airborne:mast (0.44) and airborne:aurn (0.32) are calculated as the ratio of mean airborne observations to the mast, and to the mean of all individual ground-based sites, respectively. **Right**: track of aircraft coloured by NO_2 concentration (representative of the range of the airborne data in the profile plot), with mast-based (star) and ground-based (triangles) NO_2 observations.~~

–

Figure 11: Flight M325 on 24/03/2022 from 12:09:25 to 13:46:01. Left: Altitude profile, where airborne observations of NO_2 within Greater London are shown in grey and the boxplot represents the inter-quartile range, the data range (whiskers), the median (vertical dashed black line) and mean (vertical red solid line) of these data. The London IOP supersite is shown as a black star, and AURN ground-sites within the region are shown as various

markers (see key). Ratios of airborne:mast (0.44) and airborne:aurn (0.32) are calculated as the ratio of mean airborne observations to the mast, and to the mean of all individual ground-based sites, respectively. Right: track of aircraft coloured by NO_2 concentration (representative of the range of the airborne data in the profile plot), with mast-based (star) and ground-based (triangles) NO_2 observations.

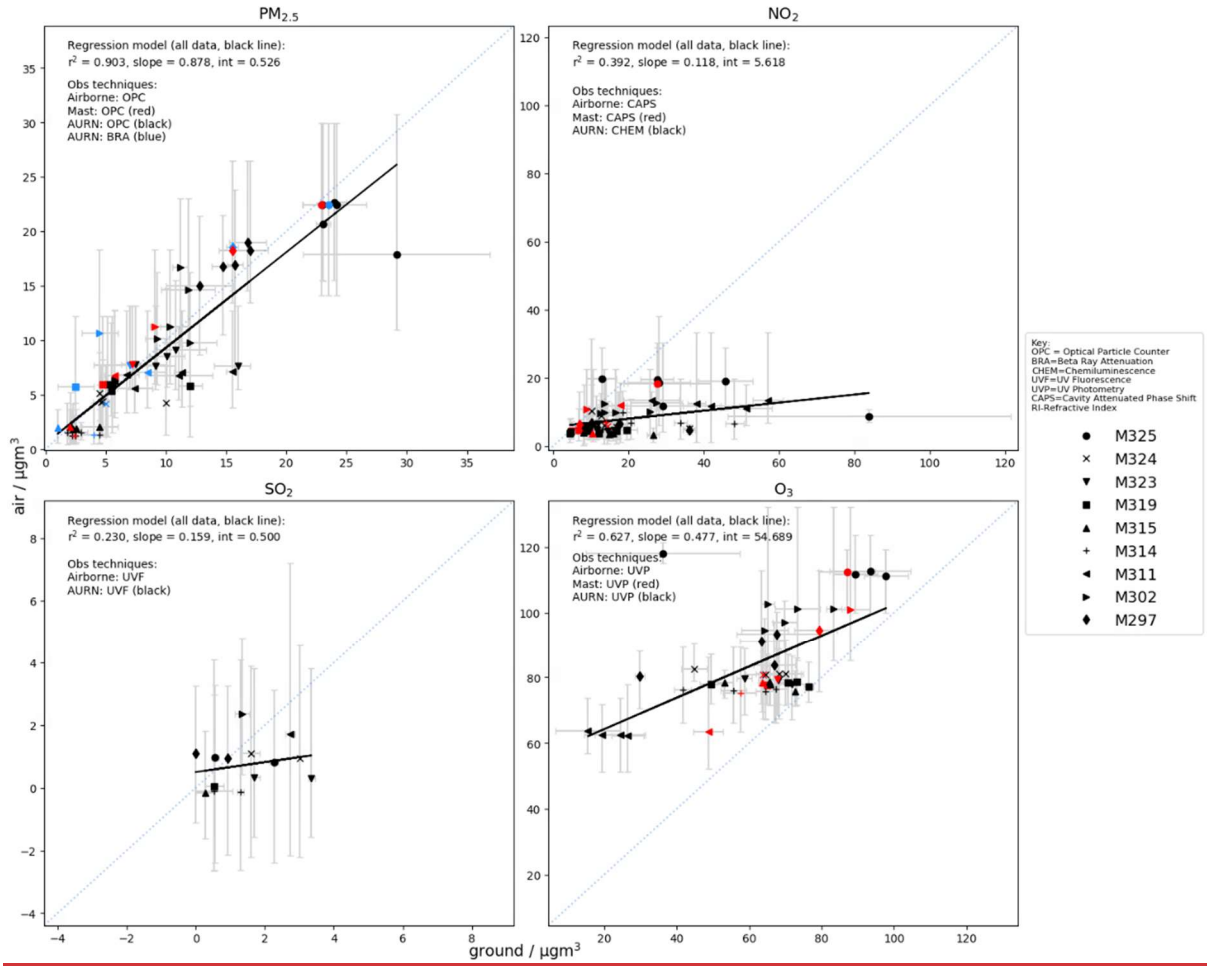
PM2.5
Regression model (all data, black line):
r² = 0.903, slope = 0.878, int = 0.526
Obs techniques:
Airborne: OPC
Mast: OPC (red)
AURN: OPC (black)
AURN: BRA (blue)
NO2
Regression model (all data, black line):
r² = 0.392, slope = 0.118, int = 5.618
Obs techniques:
Airborne: CAPS
Mast: CAPS (red)
AURN: CHEM (black)
SO2
Regression model (all data, black line):
r² = 0.230, slope = 0.159, int = 0.500
Obs techniques:
Airborne: UVF
AURN: UVF (black)
O3
Regression model (all data, black line):
r² = 0.627, slope = 0.477, int = 54.689
Obs techniques:
Airborne: UVP
Mast: UVP (red)
AURN: UVP (black)
air / µgm3
ground / µgm3
Key:
OPC = Optical Particle Counter
BRA=Beta Ray Attenuation
CHEM=Chemiluminescence
UVF=UV Fluorescence
UVP=UV Photometry
CAPS=Cavity Attenuated Phase Shift
RI-Refractive Index
M325
M324
M323
M319
M315
M314
M311
M302
M297

1235

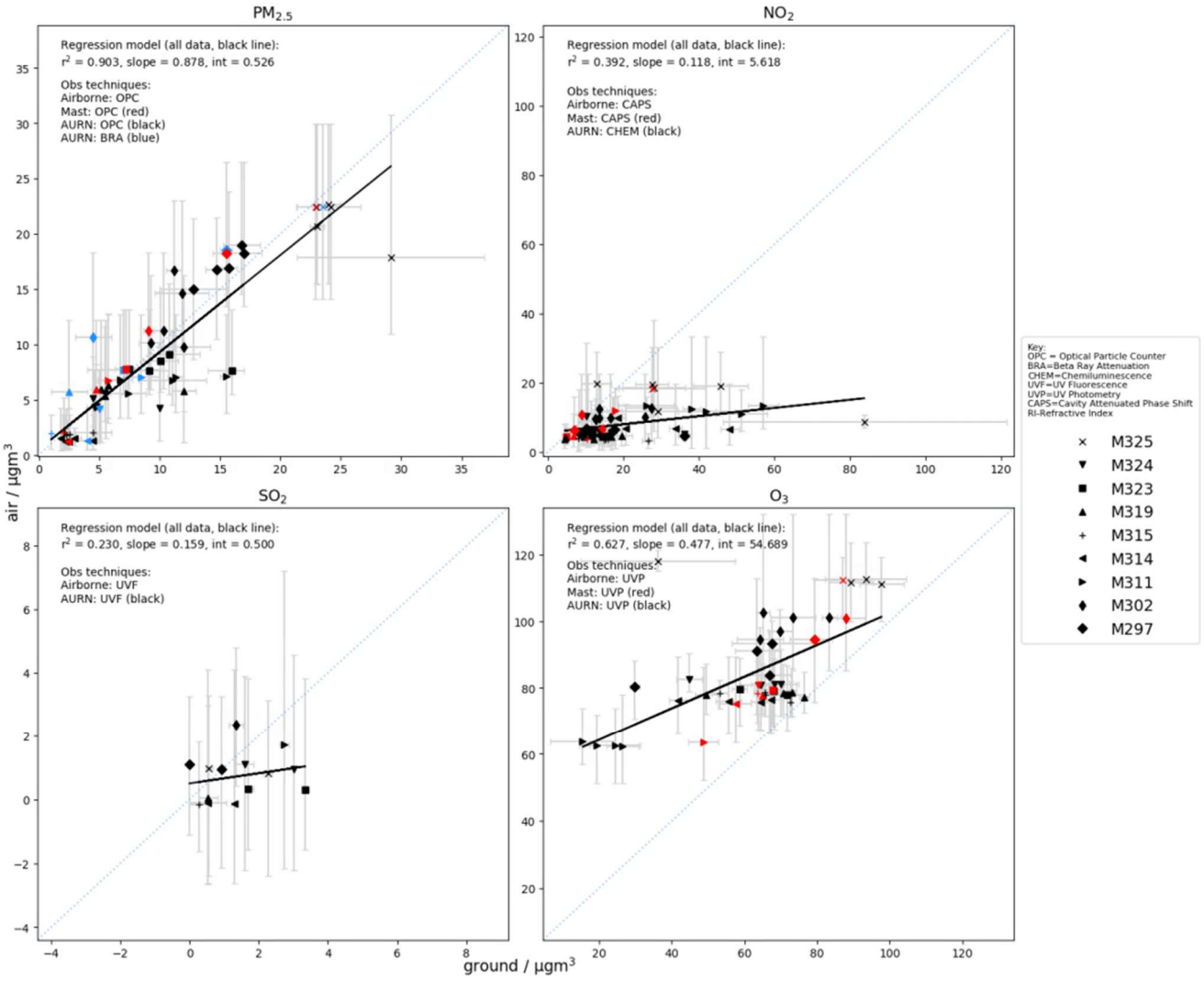

~~**Figure 13:** Average airborne observations within a 12 km radius of ground site, against local ground site average, for $PM_{2.5}$ (top left), NO_2 (top right), SO_2 (bottom left) and O_3 (bottom right), for all available London IOP flights. Comparisons against OSCA mast data are shown in red. Comparison against AURN ground-sites are shown in black for NO_2, SO_2 and O_3, and in black and blue for $PM_{2.5}$ where the different colours distinguish the different observation techniques (OPC: black and beta ray attenuation: blue). Linear regression between airborne and ground and mast based data is shown as a black line. Error bars (grey) show the range of data and the 1-2-1 line is shown as a grey dotted line.~~

Figure 12: Average airborne observations within a 12 km radius of ground site, against local ground site average, for $PM_{2.5}$ (top left), NO_2 (top right), SO_2 (bottom left) and O_3 (bottom right), for all available London IOP flights. Comparisons against OSCA mast data are shown in red and against AURN ground-sites in black. For $PM_{2.5}$, blue markers identify those AURN sites that employ Beta Ray Attenuation technique (black employs an optical particle counter with conversion to mass technique) . Linear regression between airborne and ground and mast-based data is shown in black. Error bars (grey) show the range of data and the 1-2-1 line is shown as a grey dotted line.

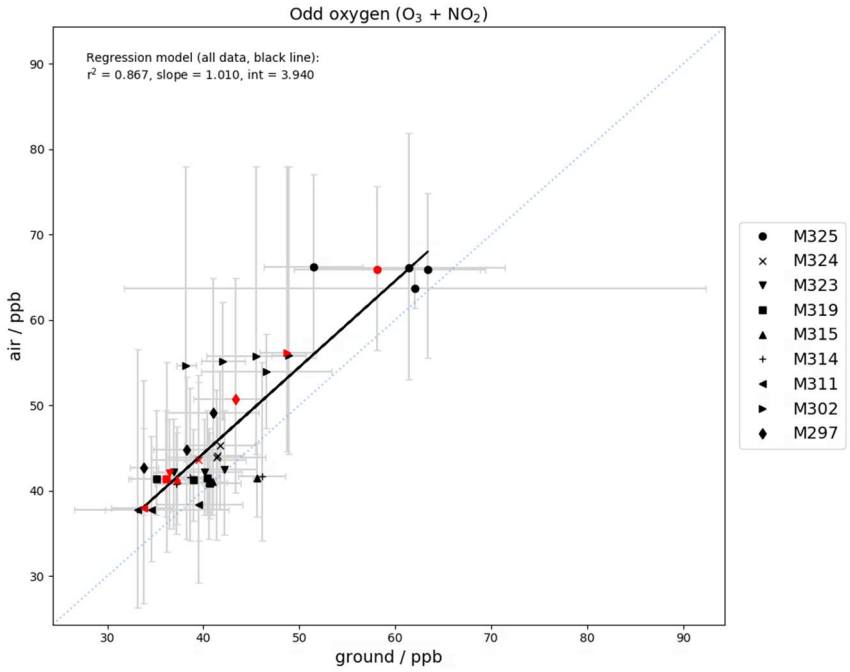

Figure 13~~14~~: odd oxygen (O_3 + NO_2 = NO) from average airborne observations of O_3 + NO_2 (in ppb) within a 12 km radius of ground site, against local ground site average O_3 + NO_2 (in ppb), for all available London IOP flights. Comparisons against OSCA mast data are shown in red, comparison against AURN ground-sites are shown in black. Linear regression between airborne and ground and mast-based data is shown as a black line. Error bars (grey) show the range of O_3 + NO_2 data and the 1-2-1 line is shown as a

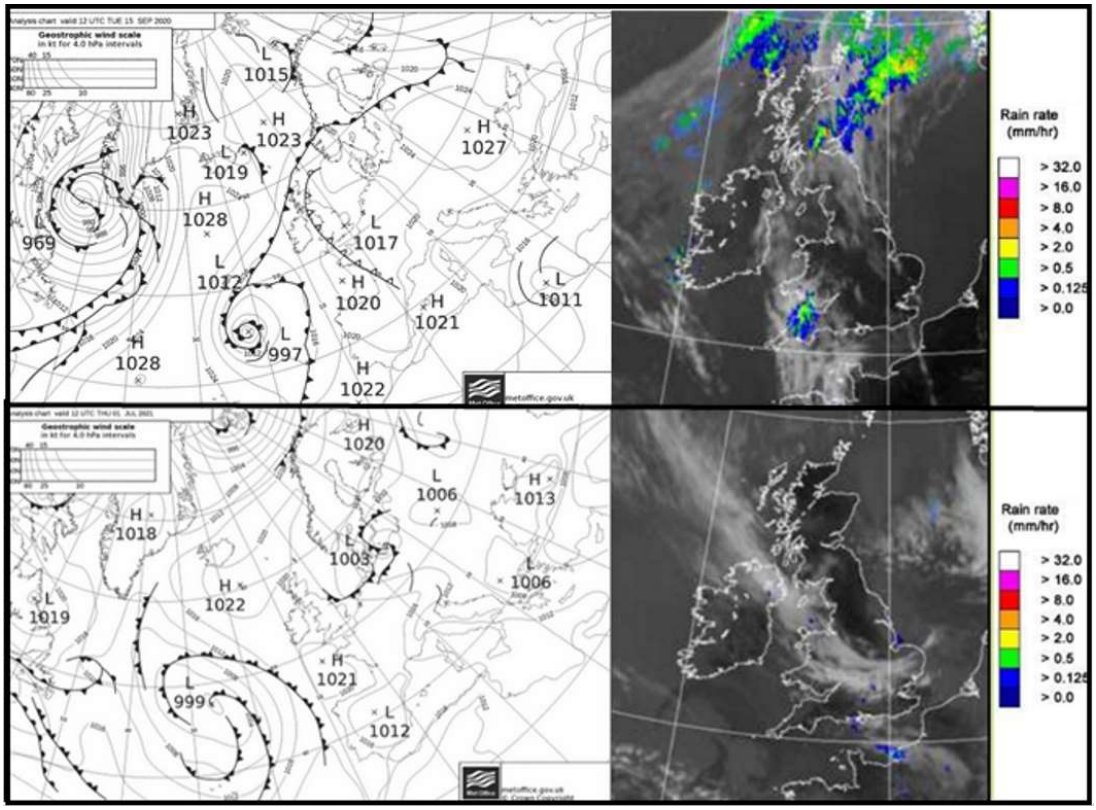

Figure 1415: Met Office synoptic chart and combined infra-red and rain-radar images for 12:00 UTC 15th September 2020 (top) and 1st July 2021 (bottom) (The National Meteorological Library, 2020).

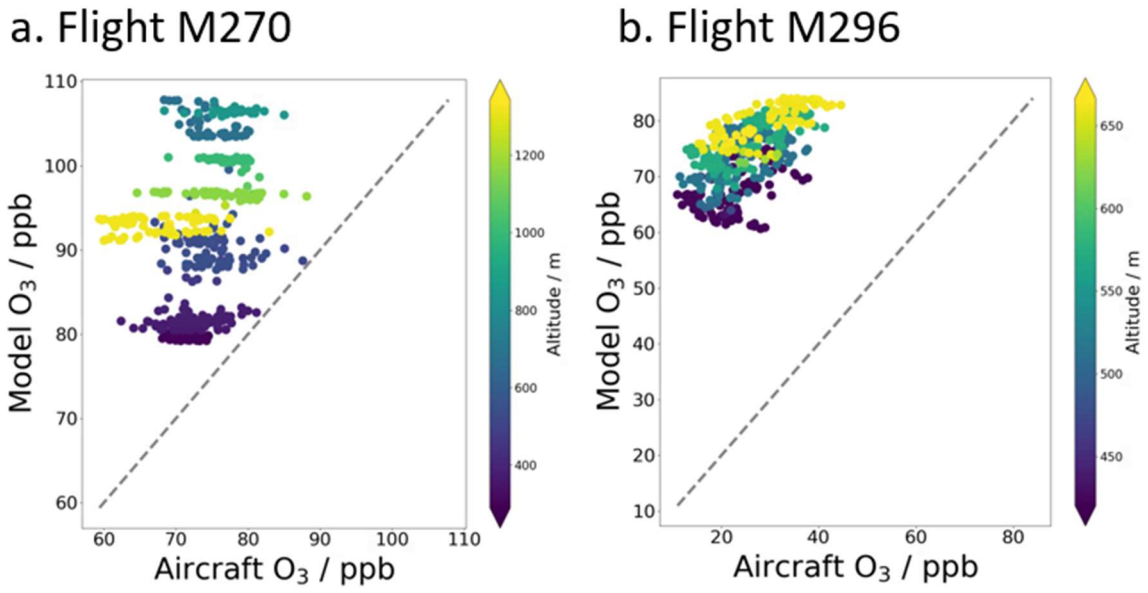

Figure 1516: Correlation of model and aircraft O_3 concentrations. Data averaged over 10 second intervals. Markers coloured by altitude. Dashed grey line represents agreement between the two datasets. Data shown for (a) Flight M270 on 15th September 2020, from 12:13:00 to 13:38:00 (the duration of the stacked level runs north

of Cambridge) and (b) Flight M296 on 1st July 2021 from 11:23:00 to 12:52:00 (the duration of the Birmingham city circuits).

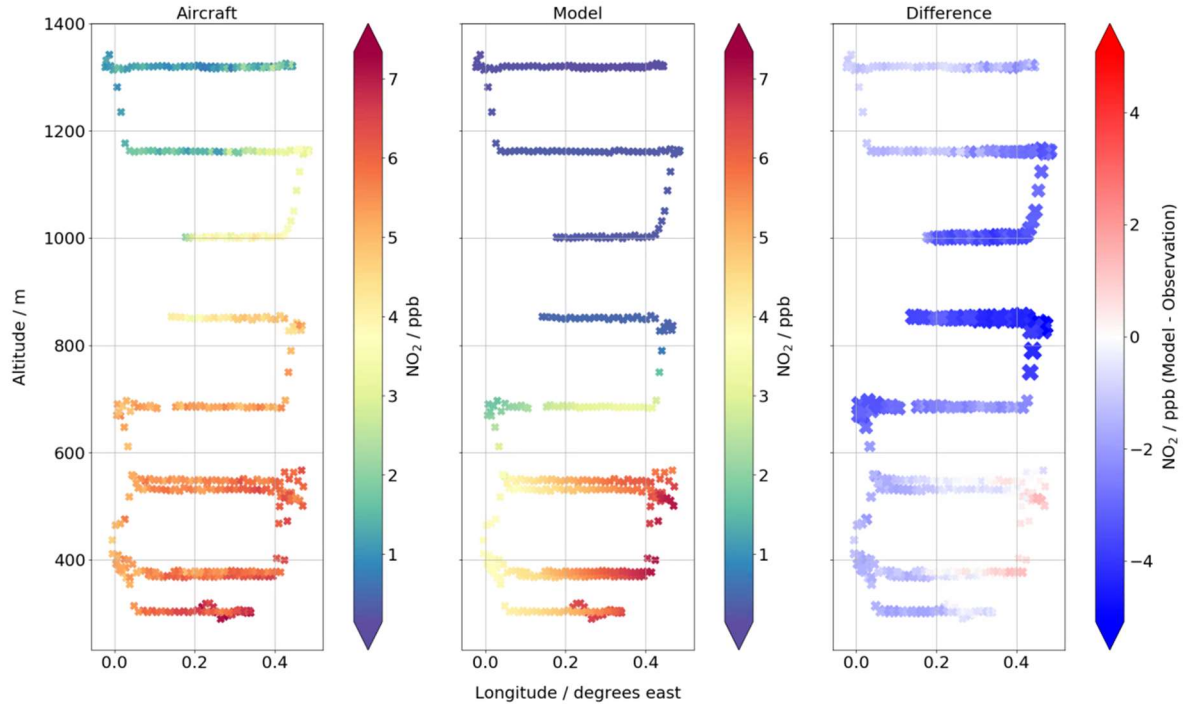

Figure 16~~17~~: Longitude-altitude plot of NO_2 concentration for vertically stacked transects during flight M270 on 15th September 2020. The left-hand figure shows the aircraft data, the middle figure shows the model data, and the right-hand figure shows the difference between the model and aircraft, where opacity and thickness increase as the difference diverges away from zero.~~.~~ Data averaged over 10 second intervals.

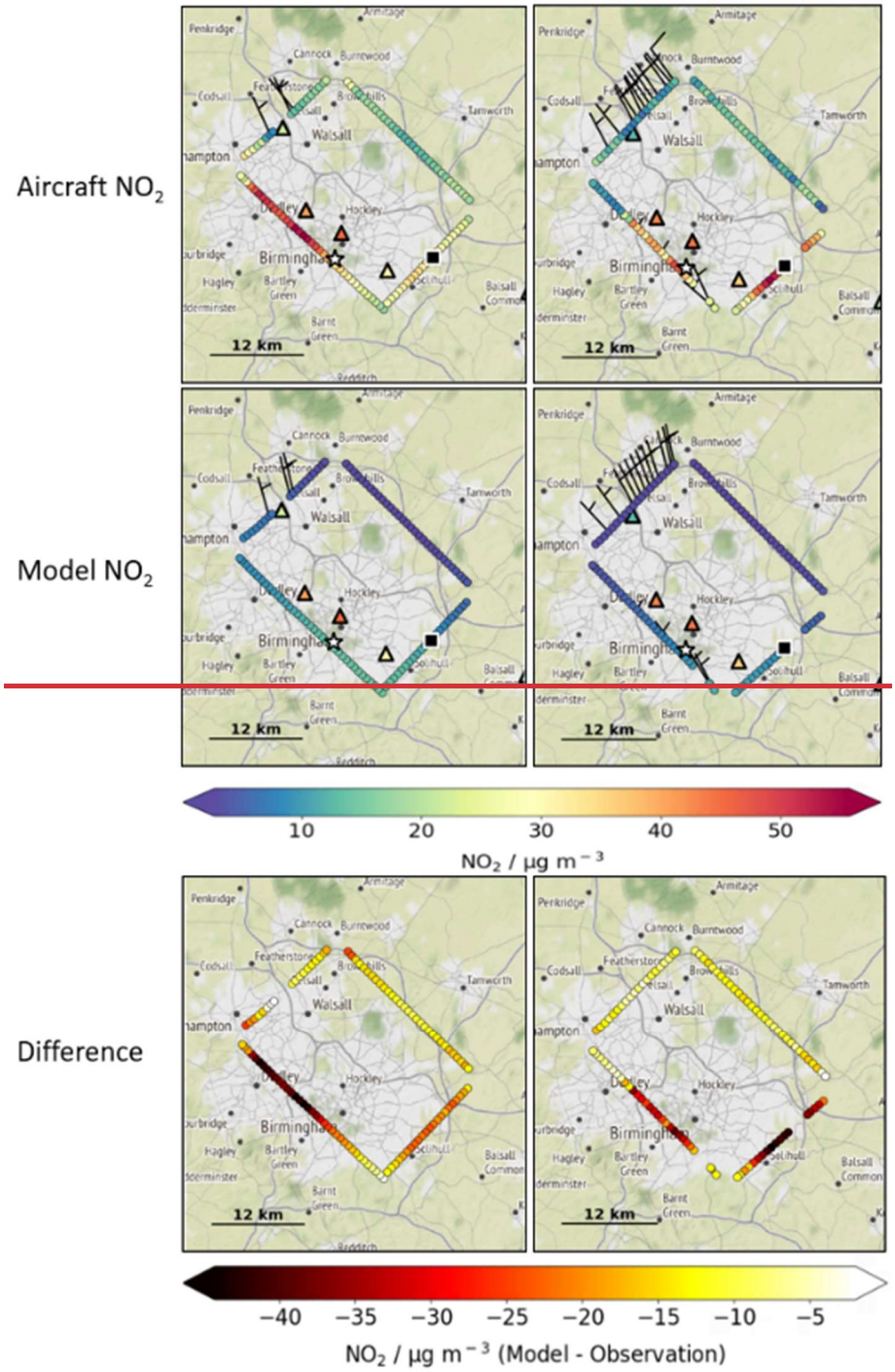

Figure 17~~18~~: Aircraft flight tracks coloured by NO_2 concentration (µg/m^3) for the first (left, 11:23 to 11:43) and fourth (right, 12:33 to 12:52) circuit, at altitudes of 423 and 657 metres, respectively, around Birmingham during flight M296 on 1st July 2021. Top row shows the aircraft data, middle row shows the model data and bottom row shows the difference between the model and observations. Observation data is from straight and wings level transects and all data is averaged over 10 second intervals. Wind barbs are only shown where the observed wind components exceed the measurement uncertainty. Data in triangles~~**boxes**~~ is the hourly surface level AURN NO_2 concentration for the circuit. Stars/squares show the location of the Birmingham supersite/airport, respectively Map tiles by Stamen Design, under CC BY 3.0. Data by OpenStreetMap, under ODbL.

Appendix figures

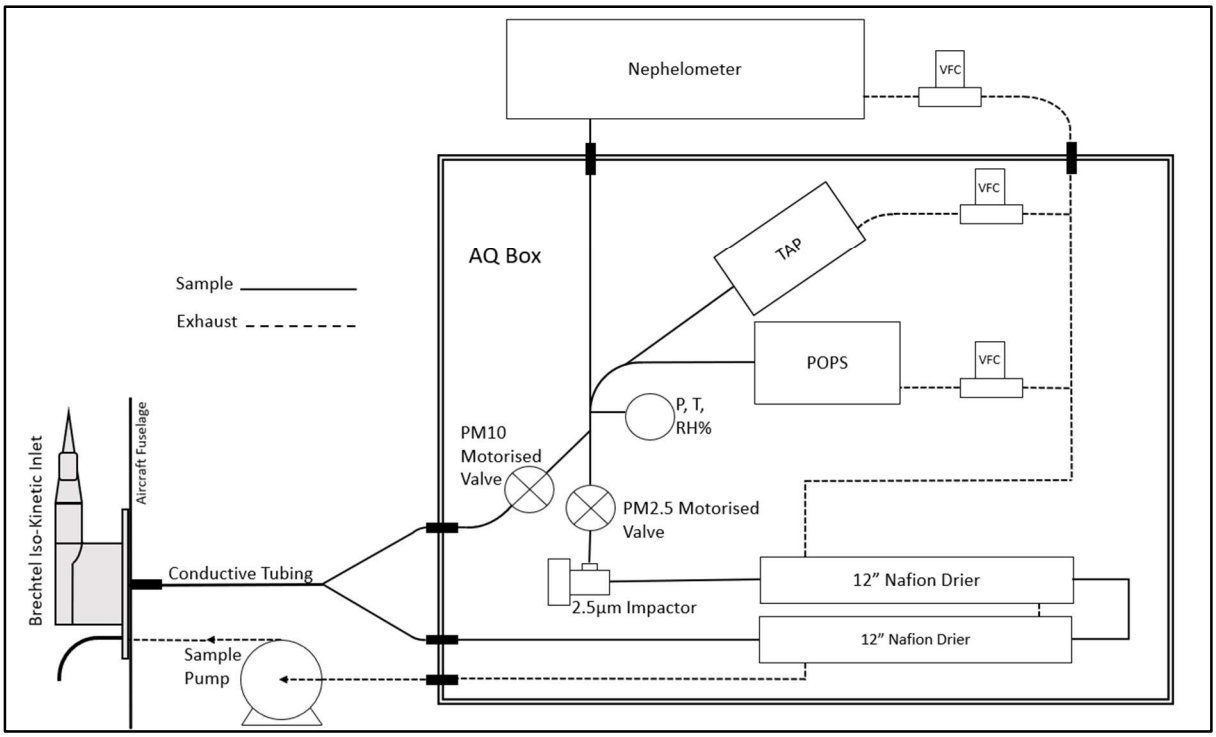

Figure A1: Air Quality box flow schematic.

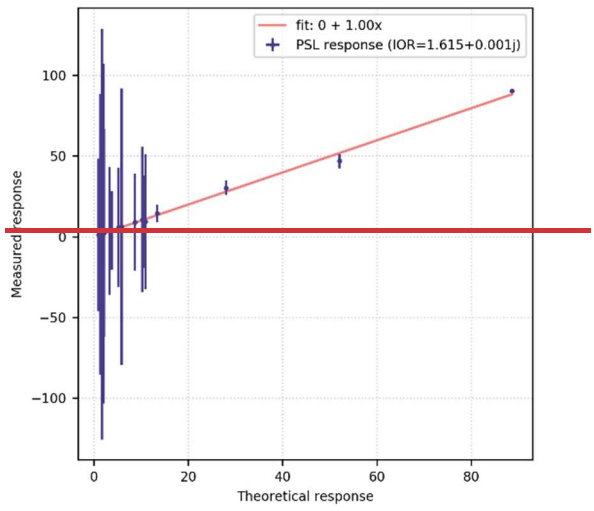

~~**Figure B1: POPS calibration from 16th September 2021. The blue circles represent PSL calibration beads with nominal diameters from 200 to 3000 nm. The vertical bars represent the error in response for each bead size and is the mean standard error of the mean for 15 second segments of each bead response.**~~

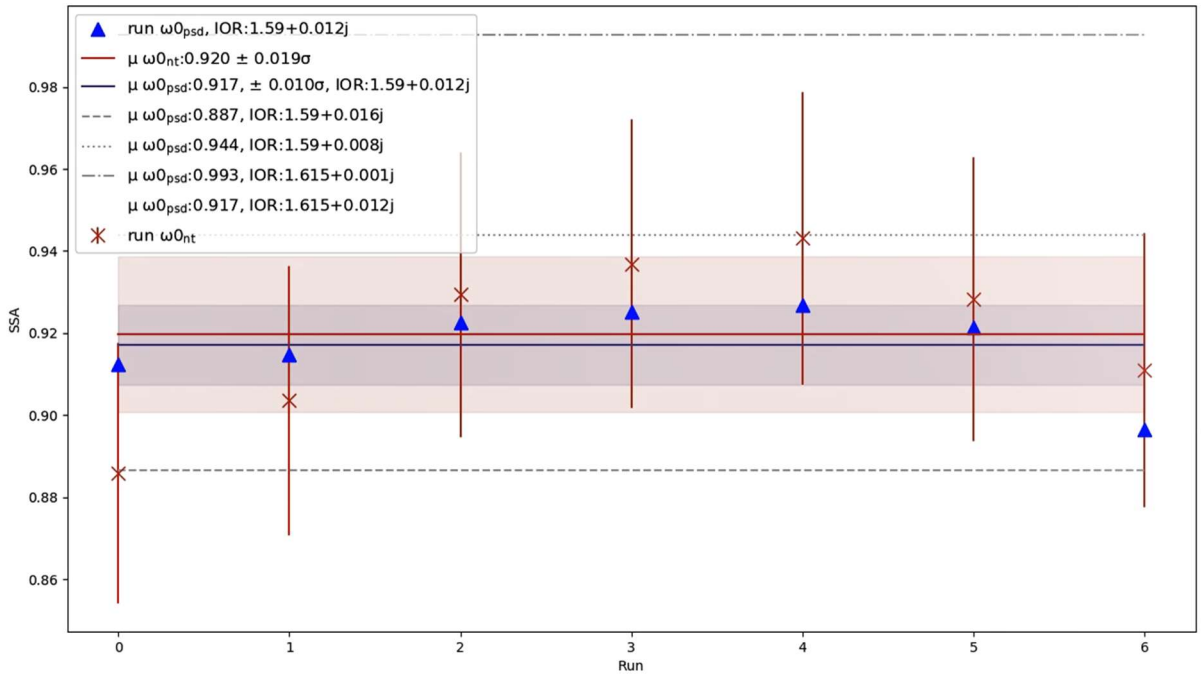

Figure B1C1: Empirically derived nephelometer and TAP single scattering albedo ($\omega 0_{nt,}$ red, crosses) and theoretically derived particle size distribution single scattering albedo ($\omega 0_{psd}$, blue, triangles) for 7 straight and level runs for flight M270 on 15th September 2021 north of Cambridge. Flight mean $\omega 0_{nt}$ and $\omega 0_{psd}$ with 1 σ variance (solid lines and shaded areas in red and blue, respectively) are shown. Also shown are the mean $\omega 0_{psd}$ derived using particle size distributions (PSD) corrected with the IOR which yielded $\omega 0_{psd}$ that closely matches the minimum $\omega 0_{nt}$ (run 0, grey dashed line) and maximum $\omega 0_{nt}$ (run 4, grey dotted line), where PSD IOR = 1.59+0.016j and 1.59+0.008j, respectively. The mean $\omega 0_{psd}$ derived using uncorrected (PSL-calibrant IOR=1.615+0.001j) PSD's is also shown (grey dot-dash line). The mean $\omega 0_{psd}$ derived using a real component of 1.615 and imaginary component of the retrieved IOR (0.12) is detailed in the legend (line not shown).

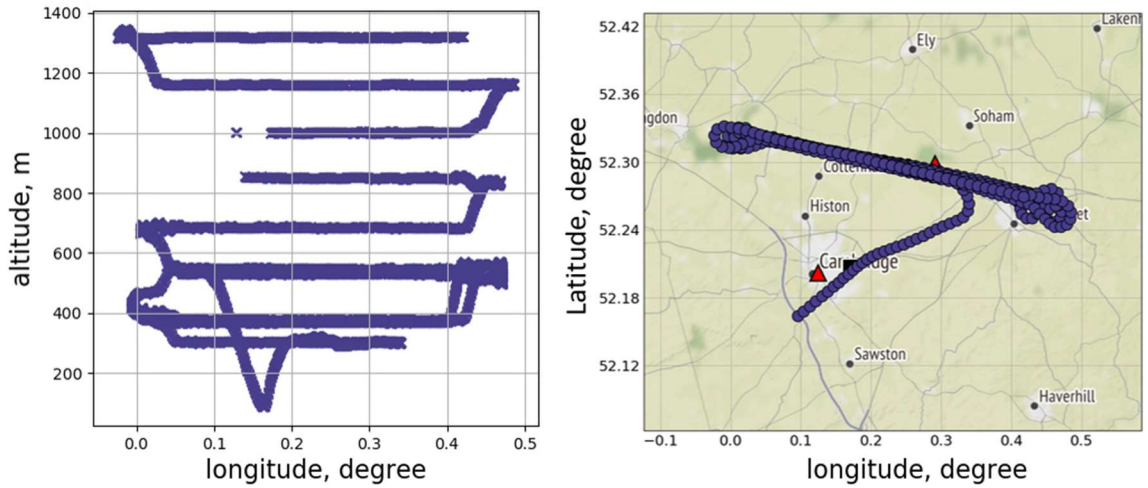

Figure B2C2: MOASA flight track for M270 north of Cambridge on 15th September 2020 in the vertical (left) and horizontal (right). Triangles are AURN sites, the square is Cambridge airport. Map tile by Stamen Design, under CC BY 3.0. Data by OpenStreetMap, under ODbL.

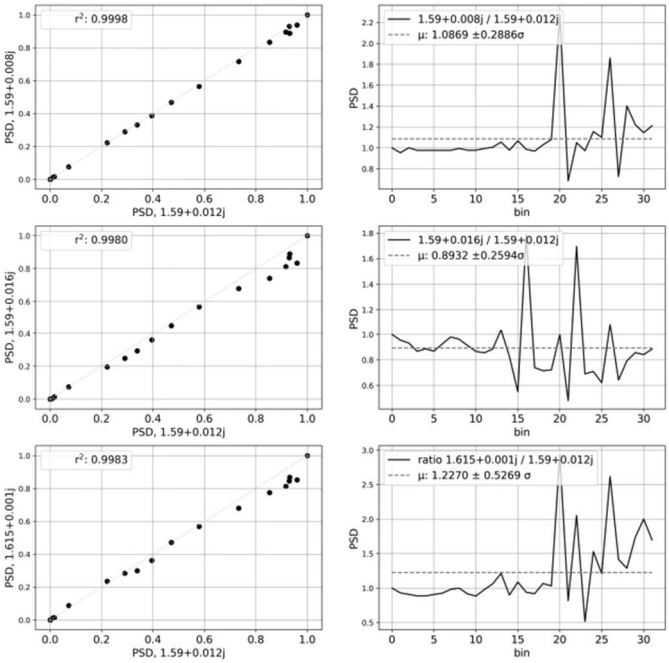

Figure B3~~C3~~: Regression analysis (left) of flight M270 run 0 normalised particle size distribution (PSD) derived using IOR=1.59+0.016j (IOR_{MIN}) against PSD derived from IOR=1.59+0.008j (IOR_{MAX}, top) and 1.615+0.001j (IOR_{PSL}) against 1.59+0.012j (IOR_{DER}, bottom). Corresponding ratios of the same PSD's are to the right.

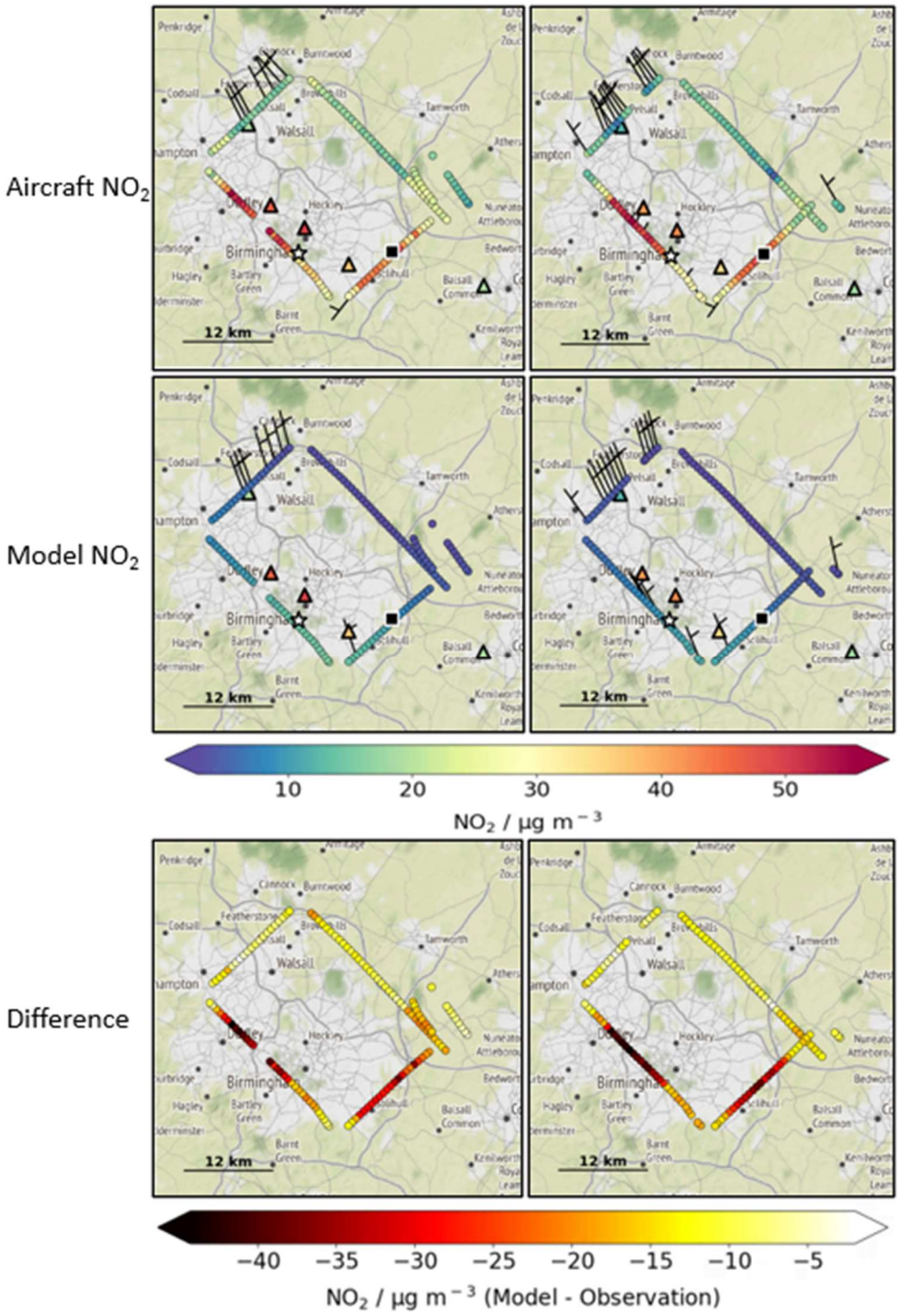

Figure D1: Aircraft flight tracks coloured by NO_2 concentration (µg/m^3) for the second (left, 11:43:00 to 12:10:00 and third (right, 12:10:00 to 12:33) circuit, at altitudes of 511 and 573 metres, respectively, around Birmingham during flight M296 on 1st July 2021. Top row shows the aircraft data, middle row shows the model data and bottom row shows the difference between the model and observations. Observation data is from straight and wings level transects and all data is averaged over 10 second intervals. Wind barbs are only shown where the observed wind components exceed the measurement uncertainty. Data in triangles is the hourly surface level AURN NO_2 concentration for the circuit. Stars/squares show the location of the Birmingham supersite/airport, respectively. Map tiles by Stamen Design, under CC BY 3.0. Data by OpenStreetMap, under ODbL

Tables

Species	Observation technique (manufacturer)	Wavelength	Range	Sensitivity
Nitrogen dioxide	Cavity Attenuated Phase Shift Spectroscopy (Aerodyne CAPS NO_2)	450 nm LED	0 - 3000 ppbv (Kebabian et al., 2005, Aerodyne Research Inc., n.d.)	0.17 ± 0.14 σ ppb
Ozone	Ultraviolet photometry (2B-Tech-205 dual-beam)	254 nm	up to 100 ppmv	2.9 ± 0.4 σ ppb
Sulphur dioxide	UV fluorescence (Thermo 43i)	Ultraviolet	0-0.05 to 100 ppm (Thermo Scientific, n.d.)	0.90 ± 0.26 σ ppb
Aerosol scattering	Multi-wavelength integrating nephelometer (Ecotech, Aurora 3000)	450nm, 525nm, 635nm	<0.25 to 2000 Mm-1	Total scattering (Mm−1): 0.05± 0.51 σ 0.10±0.55 σ 0.01±0.69 σ Total backscattering (Mm-1): 0.21± 0.95 σ 0.07± 0.49 σ 0.14±0.55 σ
Aerosol absorption	Tricolor Absorption Photometer (TAP, Brechtel, model 2901).	467, 528, 652 nm		0.22, 0.18 and 0.26 Mm−1 at wavelengths of 652, 528 and 467 nm
$PM_{2.5}$	Optical particle counter + conversion to mass concentration using iterative method (Handix POPS, (Peers et al., 2019))	405 nm	Approx. 0.1 um < d < 1 um	approximately 0.1 um < d < 1 um

Table 1: MOASA Clean Air instrument summary

Sortie Type	**Number flown**	**Flight numbers (number of designated runs in flight)**
Southwest Ground Network Survey	7	M247 (4), M256 (3), M263 (5), M266 (3), M267 (5), M286 (7), M288 (4)
Northeast Ground Network Survey	2	M253 (4), M262 (3)
South Coast Survey	5	M250, M258 (5), M265 (4), M269 (4), M301 (6)
Coastal Transition	6	M272 (3), M280 (9), M283** (N/A), M285 (11), M289 (9), M322 (N/A)
High Density Spatial Mapping	5	M257 (2), M270, Cambridge (7), M274, Dover straights (4), M281, Port Talbot (10), M284, Port Talbot (4)

London	23	M251^{NO2} (5), M252 (3), M264 (3), M273 (4), M275* (3), M276* (4), M277* (5), M278* (4), M279* (3), M282* (6), M287* (4), M294*^{iop} (5), M297*^{iop} (9), M302* (6), M305**^{NO2O3} (N/A), M311*^{iop} (4), M314*^{iop} (5), M315*^{iop} (5), M319*^{iop} (6), M323* (5), M324* (5), M325* (4), M326* (4)
Birmingham IOP	8	M290 (8), M291 (9), M295 (10), M296 (9), M310 (7), M312 (12), M313 (12), M316 (N/A),
Manchester IOP	7	M292 (7), M293 (7), M298 (5), M299 (6), M300 (6), M317 (5), M320 (6)
Total flights	**63**	

Table ~~2~~1: MOASA Clean Air flights by sortie. The numbers in brackets indicate the number of straight and level transects used to derive the index of refraction for $PM_{2.5}$ (where applicable) and (from flights M247 to M302) the analysis in Sect 4.1. "N/A" indicates that no runs were used in forward analysis. London flights which include a central overpass are postfixed with an asterisk. Flights with limited data are postfixed with a double asterisk. London flights during the ~~summer and winter~~**ground based** IOP's are also postfixed with superscript 'iop'. London flight with no NO_2 data or O_3 data are post fixed 'NO2' or 'O3' (applicable to Sect 4.4).

Run	Times	Mean altitude (m)	$\omega 0_{nt}$	$\omega 0_{psd}$ (IOR = 1.59 + 0.012j
0	12:16:20 – 12:20:20	304	0.886 ± 0.03	0.912
1	12:37:50 – 12:42:20	378	0.904 ± 0.03	0.915
2	12:52:30 – 12:57:50	686	0.929 ± 0.03	0.923
3	13:00:00 – 13:04:50	851	0.937 ± 0.04	0.925
4	13:08:40 – 13:13:10	1002	0.943 ± 0.04	0.927
5	13:16:20 – 13:21:10	1162	0.928 ± 0.03	0.921
6	13:23:50 – 13:29:20	1320	0.911 ± 0.03	0.897
	Flight averages	814.71	0.920 ± 0.019 σ	0.917 ± 0.010 σ

Table B1~~C1~~: Mean altitude and single scattering albedo derived using the nephelometer and TAP ($\omega 0_{nt}$) and particle size distributions ($\omega 0_{psd}$) for seven runs during flight M270 on 15th September 2020.

	Weighted average density (gcm^3)	**Total mass**	**Black carbon**	**Organic carbon**	**NH_4NO_3 & $NaNO_3$**	**$(NH_4)_2SO_4$**	**NaCl**	**$CaSO_4$ anhydrous**	**Fe-rich dust**	**Other (incl. bound water**

Index of refraction	-	-	1.95-0.79j [5]	1.63-0.021j [1]	NH4NO3: 1.550, 0j [6]	1.53+ 0j [1]	1.54 + 0j [3]	1.57 [8]	2.80-3.34j (Iron) [3]	1.33+ 0.0j
Density (g/cm^3)	-	-	1.8 [1]	1.35 [2]	1.72 [2]	1.77 [3]	2.17 [3]	2.96 [7]	2.5 [4]	1
Study			%	%	%	%	%	%	%	%
H2004_ub	1.69	100	14.4	25.1	14.6	21.3	2.1	1.9	10.2	10.4
H2004_ubhp	1.69	100	9.144	15.94	36.5	13.53	1.33	1.21	6.477	6.604
AG2012_ub	1.71	100	11.81	20.59	29.94	17.47	1.72	1.56	8.37	8.53
H2008_ab	1.55	100	-	24-59	20 -39	21-37	-	-	-	-
H2008_abmed	1.58	100	-	41.5	29.5	29	-	-	-	-
H2008_abmo	1.51	100	-	59	20	21	-	-	-	-
H2008_abmi	1.65	100	-	24	39	37	-	-	-	-
Mean Pp	1.64 ± 0.07 (1σ)									

Table C1~~D1~~: Average chemical composition and density (Pp, g/cm3) of UK PM2.5. Where H2004_ub and H2004_ubhp are Harrison et al., 2004 urban background and urban background high pollution, respectively. High pollution percentages represent findings by Harrison et al., 2004, who reported an approximate doubling of concentrations of elemental carbon, organic compounds, sodium nitrate, ammonium sulphate, calcium sulphate and iron-rich dusts on high pollution days, and an increase of more than five-fold in the ammonium nitrate concentration. AG2012_ub: Air Quality Expert Group, 2012 urban background, H2008_ab is Haywood, 2008, airborne measurements derived from the Facility for Airborne Atmospheric Measurements Bae146 over 3 flights (shown as reference ranges only). H2008_abmed, H2008_abmo and H2008_abmi: median, maximum organics and maximum inorganics, respectively for H2008_ab percentage ranges. Index of Refraction and Density: The numbers in square brackets refer to the reference for the associated value, which are as follows: [1] Morgan et al., 2010, [2] Haywood, 2008, [3] Hinds, 1999, [4] Lafon et al., 2006. [5] Bond and Bergstrom, 2006, [6] Hoon Jung et al., 2016, [7] CAMEO chemicals, NOAA, n.d. [8] PubChem, n.d. An assumed density of 1 ~~g/cm^3~~**gcm^3** is used for `Other including bound water'.

	~~Standard name~~ ~~Aa prefix of instrument name e.g. "NEPH_" indicates a housekeeping parameter.~~	~~Units, long name, frequency, and comments (where applicable).~~ ~~[ ] indicates a changeable parameter~~
~~Dimension~~	~~time~~	~~units: seconds since flight_date 00:00:00~~ ~~long name: the time the measurement was taken~~ ~~timezone: UTC~~ ~~frequency: 1 Hz~~

AIMMS	latitude	units: degree north long name: aircraft latitude measured by the AIMMS frequency: 1 Hz
	longitude	units: degree east long name: aircraft longitude measured by the AIMMS, frequency: 1 Hz longitude
	altitude	units: m long name: aircraft GPS height measured by the AIMMS frequency: 1 Hz comment: nominally above sea level
	air_temperature	units: K long name: ambient air temperature measured by the AIMMS frequency: 1 Hz
	relative_humidity	units: % long name: A measurement of the water vapor that exists in a mixture of air and water vapor measured by the AIMMS frequency: 1 Hz
	air_pressure	units: hPa long name: ambient air pressure measured by the AIMMS frequency: 1 Hz
	wind_speed	units: m s-1 long name: wind speed measured by the AIMMS comment: Applicable only when wings are level and wind speed is above the wind component speed threshold. Hence the wind speed flag is derived from the wind flow N flag the wind flow E flag and the roll angle flag. See config.py for the min and max limits of these parameters. frequency: 1 Hz
	wind_from_direction	units: degree long name: wind direction measured by the AIMMS comment: The direction the wind is blowing from. Applicable only when wings are level and wind speed is above the wind component speed threshold. Hence the wind direction flag is derived from the wind flow N flag the wind flow E flag and the roll angle flag. See config.py for the min and max limits of these individual parameters. frequency: 1 Hz
	roll_angle	units: degree

		long name: the rotation about the longitudinal axis of the aircraft measured by the AIMMS comment: zero degree indicates the wings on a fixed-wing aircraft are level with the local horizontal plane. frequency: 1 Hz positive: right wing down roll angle
	pitch_angle	units: degree long name: the angle between the longitudinal axis of the aircraft and the horizon measured by the AIMMS comment: zero degree indicates the nose and tail of the aircraft are level with the local horizontal plane frequency: 1 Hz positive: nose up
	true_air_speed	units: m s-1 long name: true air speed measured by the AIMMS frequency: 1 Hz
	northward_wind	units: m s-1 long name: wind flow vector north component measured by the AIMMS frequency: 1 Hz
	eastward_wind	units: m s-1 long name: wind flow vector east component measured by the AIMMS frequency: 1 Hz
	yaw_angle	units: degree long name: yaw angle as measured by the AIMMS instrument frequency: 1 Hz
	downward_air_velocity	units: m s-1 long name: vertical wind as measured by the AIMMS instrument comment: positive is down frequency: 1 Hz
	sideslip_angle	units: degree long name: angle of sideslip as measured by the AIMMS instrument frequency: 1 Hz
Nephelometer	forward_scattering_red	units: Mm-1,

		~~long name: corrected red (635nm) scattering (by gas and particles, with dark count subtracted) over 0 - 170 degrees, smoothed to 15s, measured by the Nephelometer, frequency: 1 Hz~~
	~~forward_scattering_green~~	~~units: Mm-1,~~ ~~long name: corrected green (525nm) scattering (by gas and particles, with dark count subtracted) over 0 - 170 degrees, smoothed to 15s, measured by the Nephelometer, frequency: 1 Hz,~~
	~~forward_scattering_blue~~	~~units: Mm-1,~~ ~~long name: corrected blue (450nm) scattering (by gas and particles, with dark count subtracted) over 0 - 170 degrees, smoothed to 15s, measured by the Nephelometer, frequency: 1 Hz,~~
	~~backscattering_red~~	~~units: Mm-1,~~ ~~long name: corrected red (635nm) scattering coefficient for backscatter (by gas and particles, with dark count subtracted) over 90 - 170 degrees, smoothed to 15s, measured by the Nephelometer,~~ ~~frequency: 1 Hz,~~
	~~backscattering_green~~	~~units: Mm-1,~~ ~~long name: corrected green (525nm) scattering coefficient for backscatter (by gas and particles, with dark count subtracted) over 90 - 170 degrees, smoothed to 15s, measured by the Nephelometer,~~ ~~frequency: 1 Hz~~
	~~backscattering_blue~~	~~units: Mm-1,~~ ~~long name: corrected blue (450nm) scattering coefficient for backscatter (by gas and particles, with dark count subtracted) over 90 - 170 degrees, smoothed to 15s, measured by the Nephelometer,~~ ~~frequency: 1 Hz~~
	~~scattering_correction_green~~	~~units: Mm-1~~ ~~long name: scattering corrections applied to correct raw blue scattering data measured by the Nephelometer~~ ~~frequency: 1 Hz~~
	~~scattering_correction_blue~~	~~units: Mm-1~~ ~~long name: scattering corrections applied to correct raw blue scattering data measured by the Nephelometer~~ ~~frequency: 1 Hz~~

	~~scattering_correction_red~~	~~units: Mm-1,~~ ~~long name: scattering corrections applied to correct raw red scattering data measured by the Nephelometer,~~ ~~frequency: 1 Hz~~
	~~aerosol_angstrom_exponent~~	~~units: Mm-1~~ ~~long name: Angstrom exponent as an average of wavelength pair Angstrom exponents, measured by the Nephelometer~~ ~~frequency: 1 Hz~~
	~~NEPH_sample_temperature~~	~~units: degree Celcius~~ ~~long name: sample air temperature measured by the Nephelometer~~ ~~frequency: 1 Hz~~
	~~NEPH_cell_temperature~~	~~units: degree Celcius~~ ~~long name: cell temperature measured via a sensor mounted in the cell wall (near the light source) (for the Nephelometer)~~ ~~frequency: 1 Hz~~
	~~NEPH_RH~~	~~units: %~~ ~~long name: sample air relative humidity measured by the Nephelometer~~ ~~frequency: 1 Hz~~
	~~NEPH_pressure~~	~~units: hPa~~ ~~long name: barometric pressure in the cell measured by the Nephelometer~~ ~~frequency: 1 Hz~~
	~~NEPH_flow~~	~~units: litre min-1~~ ~~long name: sample flow rate measured by the Nephelometer~~ ~~frequency: 1 Hz~~
~~TAP~~	~~absorption_coefficient_blue~~	~~units: Mm-1~~ ~~long name: Corrected (Virkkula et al, 2010) blue (wavelength = 467nm) absorption coefficient, measured by TAP.~~ ~~frequency: 1 Hz~~
	~~absorption_coefficient_green~~	~~units: Mm-1~~ ~~long name: Corrected (Virkkula et al, 2010) green (wavelength = 528nm) absorption coefficient, measured by TAP.~~ ~~frequency: 1 Hz~~

	absorption_coefficient_red	units: Mm-1 long name: Corrected (Virkkula et al, 2010) red (wavelength = 652nm) absorption coefficient, measured by TAP. frequency: 1 Hz
	TAP_sample_flow	units: litre min-1 long name: Sample flow for the TAP, as measured by TAP. frequency: 1 Hz
	TAP_sample_air_temp	units: degree Celsius long name: Sample flow for the TAP, as measured by TAP. Frequency: 1 Hz
	TAP_case_temp	units: degree Celsius long name: Case temperature for the TAP, as measured by TAP. frequency: 1 Hz
POPS	mass_concentration_of_dried_pm2p5_aerosol_in_air	units: µg m-3 long name: Mass concentration of dried pm2p5 aerosol in air for the POPS instrument frequency: 1 Hz comment: assumes homogeneous spherical particles and a density of [density] g/cm^3. Calculated using index of refraction [IOR] corrected, calibrated mid-bin diameters from the POPS instrument. Diameter range used in PM2.5 calculations: [lower bin] µm to [upper bin] µm. Sample is dried (relative humidity typically below 20%).
	number_concentration_of_aerosol	units: cm3 long name: number concentration of aerosol measured by the POPS instrument frequency: 1 Hz
	aerosol_particle_counts	units: counts s-1 long name: particle counts measured by the POPS instrument frequency: 1 Hz
	dried_aerosol_size_spectra	units: counts long name: number of dried particle counts per bin for the POPS instrument frequency: 1 Hz
	bin_boundaries	units: nm,

		long name: nominal and calibrated bin boundaries in terms of scattering cross section, and nominal, calibrated and calibrated IOR corrected bin boundaries in terms of diameter for the POPS instrument. See comment for key., frequency: N/A, comment: Index for rows (1 to 16) are: lr_ss, ur_ss, mbr_ss, mbr_ss_err, lr_d, ur_d, mbr_d, mbr_d_err, lc_ss, uc_ss, mbc_ss, mbc_ss_err, lc_d, uc_d, mbc_d, mbc_d_err where l=lower, u=upper, mb=mid bin, ss=scattering_signal, d=diameter, r=raw, c=calibrated, err=error}
	POPS_sample_flow	units: cm3 s-1 long name: sample flow rate measured by the POPS instrument frequency: 1 Hz comment: measured by the laminar flow element and differential pressure sensor on the POPS instrument,
	POPS_bl	unit: counts long name: baseline of the detector (raw analog-to-digital counts) measured by the POPS instrument frequency: 1 Hz
	POPS_blth	units: N/A long name: baseline threshold for particle counting frequency: 1 Hz
	POPS_laserdiode_temp	units: degree Celcius long name: temperature of laser diode control board measured by the POPS instrument frequency: 1 Hz
	POPS_ld_mon	unit: arbitrary value long name: laser diode output power monitor measured by the POPS instrument frequency: 1 Hz
	POPS_laserfb	unit: arbitrary value long name: feedback value used when controlling laser power using PID control measured by the POPS instrument frequency: 1 Hz
	POPS_ambient_pressure	units: hPa long name: ambient pressure as measured by the POPS instrument frequency: 1 Hz

	POPS_pumpfb	unit: arbitrary value long name: feedback value used when controlling pump speed using PID control measured by the POPS instrument frequency: 1 Hz
	POPS_onboard_temp	units: degree Celcius long name: on-board temperature measured by the POPS instrument frequency: 1 Hz
NO2	mass_concentration_of_nitrogen_dioxide_in_air	units: µ m-3 long name: manually calculated nitrogen dioxide concentration with manual baseline subtracted, as measured by the NO2 instrument frequency: 1 Hz
	concentration_of_nitrogen_dioxide_in_air	units: ppbv long name': manually calculated nitrogen dioxide concentration with manual baseline subtracted, as measured by the NO2 instrument frequency: 1 Hz
	NO2_manual_baseline	units: Mm-1 long name: baseline used in manual concentration calculation of NO2. frequency: 1 Hz
	NO2_man_baseline_1	units: Mm-1 long name: manually calculated baseline method 1 (for the NO2 instrument) comment: derived by linearly interpolating between consecutive baseline measurements. frequency: 1 Hz
	NO2_man_baseline_2	units: Mm-1 long name: manually calculated baseline method 2 (for the NO2 instrument) comment: derived using defined scaling of Rayleigh corrected baseline loss (Mm-1) per mb to determine baseline based on NO2 cell pressure frequency: 1 Hz
	NO2_man_baseline_3	units: Mm-1 long name: manually calculated baseline method 3, as per method 2, but do a linear fit to pressure dependence of background only when pressure span is bigger than 250 mb (for the NO2 instrument)

		frequency: 1 Hz
	NO2_cell_pressure	units: hPa long name: cell pressure measured by the NO2 instrument frequency: 1 Hz
	NO2_cell_temperature	units: K long name: cell temperature measured by the NO2 instrument frequency: 1 Hz
	NO2_N	units: cm-3 long name: nitrogen dioxide molecular number density calculated at sensor pressure and temperature (for the NO2 instrument) frequency: 1 Hz
O3	mass_concentration_of_ozone_in_air	units: µg m-3, long name: mass concentration of ozone measured by the ozone instrument frequency: 0.5 Hz
	concentration_of_ozone_in_air	units: ppbv long name: concentration of ozone measured by the ozone instrument frequency: 0.5 Hz
	O3_cell_pressure	units: hPa long name: measurement cell pressure measured by the ozone instrument frequency: 0.5 Hz
	O3_cell_temperature	units: degree_Celsius long name: measurement cell temperature measured by the ozone instrument frequency: 0.5 Hz
	O3_volumetric_flow_rate	units: cm3 min-1 long name: volumetric flow rate measured by the ozone instrument frequency: 0.5 Hz
SO_2	mass_concentration_of_sulfur_dioxide_in_air	units: µg m-3 long name: mass_concentration_of_sulfur_dioxide_measured_by_the_SO2_instrument frequency: 1 Hz comment: minimum detection limit ± 2.661 µg m-3. Be aware of signal to noise at low concentrations

	concentration_of_sulfur_dioxide_in_air	units: ppbv long name: sulfur dioxide concentration measured by the SO2 instrument frequency: 1 Hz comment: minimum detection limit ± 1PPB. Be aware of signal to noise at low concentrations
	SO2_internal_temperature	units: degree_Celsius long name: internal temperature measured by the SO2 instrument frequency: 1 Hz
	SO2_reaction_temperature	units: degree_Celsius long name: reaction (or chamber) temperature measured by the SO2 instrument frequency: 1 Hz
	SO2_pressure	units: hPa long name: reaction chamber pressure measured by the SO2 instrument frequency: 1 Hz
	SO2_flow	units: litre min-1 long name: sample flow measured by the SO2 instrument frequency: 1 Hz

Table F1: Units, description (long name) and frequency of Clean Air NetCDF variables.